International Journal of Nanomedicine

Dovepress
Taylor & Francis Group

Open Access Full Text Article

ORIGINAL RESEARCH

Strain-Specific *Bacillus subtilis*-Derived Silver Nanoparticles for Effective Antibacterial Activity Against Multidrug-Resistant Pathogens: In Vitro Model

Priyanka Singh[1], Ivan Mijakovic[1,2]

[1]The Novo Nordisk Foundation, Center for Biosustainability, Technical University of Denmark, Kogens Lyngby, DK-2800, Denmark; [2]Systems and Synthetic Biology Division, Department of Biology and Biological Engineering, Chalmers University of Technology, Gothenburg, SE-412 96, Sweden

Correspondence: Priyanka Singh; Ivan Mijakovic, Email prisin@biosustain.dtu.dk; ivan.mijakovic@chalmers.se

Introduction: Nanoparticles, particularly silver and gold nanoparticles, have emerged as powerful tools for improving drug stability, bioavailability, and targeted delivery in medical applications. With the increasing global demand for nanoparticles (NPs), sustainable and biocompatible production methods are crucial. This study investigates the biosynthesis of silver nanoparticles (AgNPs) and gold nanoparticles (AuNPs) using two genetically related bacterial strains, *Bacillus subtilis* 168 and *Bacillus subtilis* 3610, and compares their synthesis efficiency and the antimicrobial potential of the generated NPs.

Methods: AgNPs were synthesized extracellularly from bacterial cell supernatants, whereas AuNPs were generated intracellularly by incubating washed cell pellets with gold salt. The nanoparticles were characterized using UV–Vis spectroscopy, sp-ICP-MS, TGA, SEM, TEM, FTIR, MALDI-TOF, zeta potential, and AFM. Antibacterial activity against *Pseudomonas aeruginosa* and *Escherichia coli* was evaluated using minimum bactericidal concentration (MBC) assays, live/dead fluorescence staining, and SEM-based morphological analysis.

Results: Both strains synthesized AgNPs and AuNPs, but *Bacillus subtilis* 3610 exhibited faster and more efficient production. AgNPs displayed uniform spherical morphology, whereas AuNPs were polydisperse and membrane-associated. AgNPs synthesis was completed within 2 days by strain 3610 compared with 3 days by strain 168. Antibacterial assays revealed markedly stronger efficacy of 3610-derived AgNPs, with MBC values of 2 µg/mL against *P. aeruginosa* and 8 µg/mL against *E. coli*, in contrast to 16 µg/mL and 32 µg/mL, respectively, for 168-derived AgNPs.

Conclusion: This study highlights the superior NPs biosynthesis capacity and antibacterial potency of the wild-type strain *B. subtilis* 3610 compared to the domesticated laboratory strain 168. The findings emphasize the critical influence of strain-specific genetic and metabolic traits in optimizing microbial nanomaterial production and position 3610-derived AgNPs as promising candidates for biomedical applications.

Keywords: *B. subtilis*, silver nanoparticles, gold nanoparticles, simultaneous production, antimicrobial resistance, multidrug-resistant pathogens, stability

Introduction

Nanoparticles (NPs) lie at the intersection of physics, chemistry, and biology, representing a transformative frontier in scientific and technological innovation.[1] These nanoscale structures exhibit properties distinct from their bulk counterparts due to size and shape-dependent effects, leading to unique physicochemical behaviors.[2] At this scale, material properties are strongly influenced by size, shape, and the amplified surface-to-volume ratio, which imparts enhanced reactivity, optical features, and performance compared to bulk materials.[3] In particular, surface plasmon resonance (SPR) contributes distinctive optical properties, making these NPs invaluable in biomedical applications such as imaging, diagnostics, and therapeutics.[4]

Received: 12 March 2025
Accepted: 7 October 2025
Published: 29 October 2025

Graphical Abstract

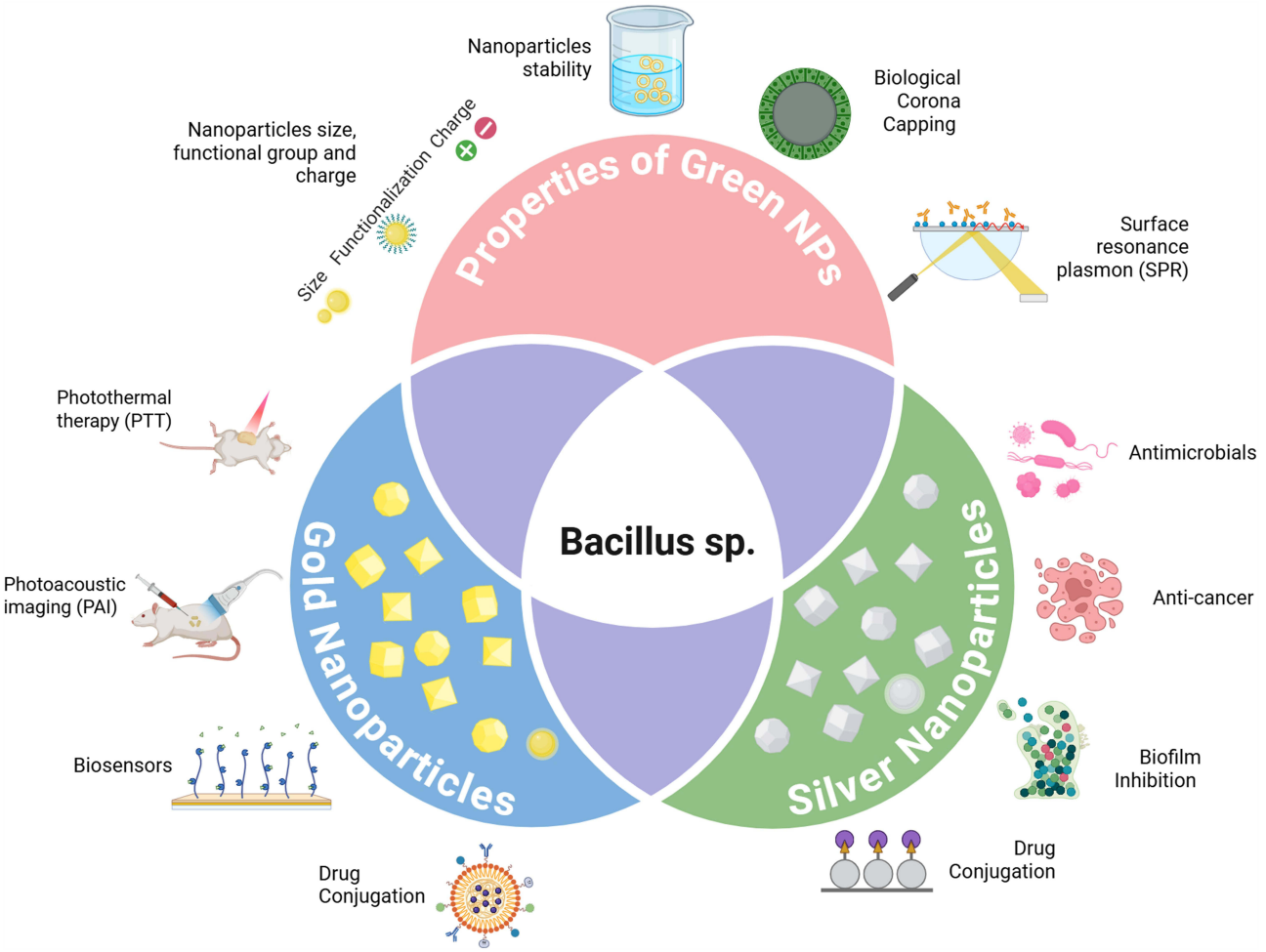

Among metallic NPs, silver nanoparticles (AgNPs) and gold nanoparticles (AuNPs) have garnered significant attention because of their remarkable physicochemical attributes and broad biomedical applications.[5,6] AgNPs, beyond their well-known antimicrobial activity, present numerous advantages in the medical landscape.[7] Their biocompatibility and the capacity to modulate size and shape position them as ideal candidates for targeted drug delivery, anti-inflammatory, antimicrobial, wound healing, anticancer, and antidiabetic therapies.[8]

AuNPs, characterized by unique SPR-dependent optical properties, herald a new era in diagnostics and medical imaging.[9] The distinctive SPR of AuNPs facilitates enhanced contrast in imaging modalities such as computed tomography (CT) and magnetic resonance imaging (MRI).[10–12] AuNPs also function as carriers for targeted drug delivery, selectively transporting therapeutics to cancer cells while sparing healthy tissues. Importantly, several AuNPs-based formulations have already advanced into clinical trials, underscoring their translational potential. Other metal-based NPs such as zinc oxide (ZnO), titanium dioxide (TiO_2), and copper nanoparticles (CuNPs) also show antimicrobial and anticancer potential.[13,14] Nevertheless, AgNPs and AuNPs remain the most widely studied because of their high surface reactivity, established medical value, and compatibility with green synthesis approaches. Meeting the rising demand for these NPs requires sustainable and scalable production strategies.[15]

To address the sustainable demand for these NPs, green routes, specifically biological synthesis, offer an environmentally friendly alternative to conventional chemical methods.[16–18] With their diverse metabolic capabilities, bacteria stand out as efficient nanofactories for metallic NPs production.[19,20] Several bacterial species have been explored for the biosynthesis of green NPs, including *E. coli, Pseudomonas putida, B. subtilis, Lactobacillus spp., Streptomyces spp*., and *Klebsiella pneumoniae*. These microorganisms act as natural reducing and stabilizing agents. Among them, *Bacillus* species are especially attractive due to their robustness, adaptability, and well-characterized enzymatic systems, enabling cost-effective, scalable, and environmentally sustainable NPs synthesis.[21] Notably, closely related *Bacillus* strains can exhibit substantial physiological and metabolic differences that influence NPs biosynthesis. For example, *B. subtilis* 168 and *B. subtilis* 3610, though genetically related, differ in traits such as biofilm formation, motility, and enzyme secretion. These differences provide a unique opportunity to evaluate how strain-specific characteristics govern NPs yield, stability, and morphology.[22]

Addressing antimicrobial resistance (AMR) remains a global health priority, as the growing resistance of pathogenic bacteria to antibiotics poses an urgent threat.[23] AgNPs have emerged as promising candidates due to their multifaceted antibacterial mechanisms, including membrane disruption, reactive oxygen species (ROS) generation, and silver ion (Ag +) release, which collectively bypass conventional resistance pathways.[24–26] In this study, we selected *P. aeruginosa* PAO1 and *E. coli* UTI89, two clinically relevant multidrug-resistant strains, to assess the antimicrobial efficacy of green AgNPs. Antibacterial potential was evaluated using plate count assays, live/dead staining for membrane integrity, and SEM. This comprehensive approach provides mechanistic insight into the bactericidal activity of generated AgNPs.[27]

Materials and Methods

Analytical-grade silver nitrate ($AgNO_3$) and gold(III) chloride trihydrate ($HAuCl_4 \cdot 3H_2O$) were sourced from Sigma-Aldrich Chemicals (St. Louis, MO, USA) for the synthesis of NPs using *B. subtilis* 168 and *B. subtilis* 3610 bacterial strains.

Biosynthesis of AgNPs and AuNPs From B168 and B3610 Strains

B. subtilis 168 and *B. subtilis* 3610 strains were obtained from the Novo Nordisk Foundation Center for Biosustainability. Strain B168 is a well-characterized lab-adapted mutant, while B3610 represents a wild-type strain with natural motility and biofilm-forming characteristics. To synthesize AgNPs, 24 h of cultures of these strains were centrifuged at 8000 rpm for 5 min to separate the pellets. The supernatant was further incubated with 1 mM silver nitrate at 37°C for 24–72 h and monitored for color change in the medium.[28] The same pellets were washed three times with PBS and incubated with 1 mM gold salt at 250 rpm and 37°C for the next 24–72 h for AuNPs production. The pellet was also observed for color change with time, and data was recorded. All experiments were performed in triplicate (n=3 biological replicates and n=3 technical replicates).

Characterization of NPs

UV-Vis Spectroscopy

UV-Vis spectroscopy, performed with the JENWAY 6705 UV-Vis spectrophotometer, monitored the reduction of metal ions. The synthesized pure NPs were suspended in water for subsequent analytical characterization.[29]

Single-Particle ICP-MS (Sp-ICP-MS)

To quantify the concentration of the synthesized NPs, sp-ICP–MS was performed using a NexION 350D instrument (PerkinElmer Inc., Waltham, MA, USA). The analysis followed established protocols reported in previous study.[30]

Stability and Thermogravimetric Analysis

The stability of the NPs was systematically assessed at varying time intervals, temperatures, and in different bacteriological media, including Tryptic Soy Broth (TSB) and Luria Broth (LB). Stability was evaluated through visual inspection, UV–Vis spectroscopy, and sp-ICP–MS before and after incubation periods. Visual observations were

documented with images to capture physical changes, aggregation, or dispersion. UV–Vis spectroscopy was used to monitor optical property changes, while sp-ICP–MS provided quantitative concentration data, enabling a comprehensive stability profile. Thermogravimetric analysis (TGA) (TA Instruments, New Castle, DE, USA) was also performed. NPs were air-dried into pellets, placed in alumina pans, and heated from 20 to 700 °C at 10 °C/min.[31]

Electron Microscopy (SEM, TEM, EDX)

The morphology and elemental composition of NPs were examined using scanning electron microscopy (SEM) coupled with energy-dispersive X-ray spectroscopy (EDX). The SEM analysis was performed on a FEI Quanta 200 FEG ESEM (Thermo Fisher Scientific).[32] For sample preparation, 5 µL of pure NPs solution (0.1 mg/mL) was deposited onto a carbon tape and air-dried at room temperature (RT) for 15 min. This method ensured uniform distribution of the NPs on the substrate, facilitating accurate analysis. SEM micrographs were then captured to visualize the NPs' morphology, size distribution, and elemental composition with surface morphology. Additionally, EDX analysis was performed to determine the elemental composition of the NPs. This setup allowed for comprehensive characterization, providing insights into their structure and chemical composition. Transmission electron microscopy (TEM) analysis, conducted with the FEI Tecnai T20 G2, offered detailed structural morphology.[33] Utilizing TEM, an in-depth analysis of the internal morphology, composition, and crystallographic details of NPs was conducted; the TEM instrument operated at an acceleration voltage of 200 kV, enabling high-resolution imaging and detailed characterization. A drop of the pure NPs solution, suspended in water, was carefully placed onto a carbon-coated copper grid to prepare the sample. Subsequently, the sample-loaded grid underwent a thorough drying process, ensuring the removal of any residual solvent and maintaining the stability of the NPs on the grid. The high acceleration voltage provided by the TEM instrument facilitated the examination of the internal structure of NPs at a nanoscale level, offering valuable insights into their morphology, elemental composition, and crystalline properties. Using a carbon-coated copper grid provided a suitable substrate for the NPs, enhancing the quality and reliability of the TEM analysis.

Surface Characterization by FTIR Spectroscopy

Fourier transform infrared (FTIR) analysis was employed to elucidate the presence of biomolecules and identify functional groups responsible for NPs formation, capping, and stabilization. The FTIR measurements were conducted using a Nicolet iS50 instrument from Thermo Fisher Scientific, Waltham, MA, USA. The analysis involved scanning air-dried purified AgNPs and freeze-dried cell supernatant over the 500–4000 cm^{-1} spectral range. The Nicolet iS50 instrument recorded spectra during the analysis, presenting the data as transmittance (%) plotted against wavenumber (cm^{-1}). This approach allowed for a comprehensive examination of molecular vibrations and absorption bands within the NPs and the cell supernatant. The FTIR spectra provided valuable information regarding the biomolecular composition and functional moieties involved in NPs synthesis, and stabilization.

Surface Characterization by MALDI-TOF Mass Spectrometry

The surface characteristics of NPs were investigated using MALDI-TOF. Purified NPs (1 µL) were applied onto an AnchorChipTM target plate (Bruker-Daltonics, Bremen, Germany), followed by the addition of 1 µL of matrix solution (0.5 mg/mL 2,5-dihydroxybenzoic acid in 90% (v/v) acetonitrile, 0.1% (v/v) trifluoroacetic acid (TFA)), and washed with 0.5% (v/v) TFA. The analyses were conducted using a MALDI-TOF mass spectrometer (Ultraflex II, Bruker-Daltonics, Bremen, Germany) in positive ion reflector mode, with 1000 laser shots per spectrum, utilizing Flex Control v3.4. Subsequently, the acquired spectra were processed using Flex Analysis v3.0 (Bruker-Daltonics, Bremen, Germany), with mass calibration performed employing protein standards (tryptic digest of β-lactoglobulin, 5 pmol/µL).

Zeta Potential and AFM Analysis

Zeta potential of NPs was analyzed as reported previously.[34] Atomic force microscopy (AFM) measurements were conducted using the Park NX20 system. The AFM operated in intermittent contact mode, utilizing standard probes made of single-crystal highly doped silicon featuring a radius of curvature of less than 30 nm (SuperSharpSiliconTM Non-

Contact AFM probes from Nanosensors). The standard uncertainty (u(d)) associated with the measured diameter was less than 5% of the diameter (u(d) < 0.05 d).

The Antibacterial Activity of AgNPs Using in vitro Model

Plate Count Assay

To evaluate the antibacterial activity of AgNPs synthesized from *B. subtilis* 168 and 3610, a plate assay was conducted using *Pseudomonas aeruginosa* PAO1 and *Escherichia coli* UTI89. Overnight bacterial cultures were diluted to ~10^7 CFU/mL (OD600 = 0.1) in LB broth, and 900 µL of this suspension was mixed with AgNPs to achieve final concentrations ranging from 0.1 to 32 µg/mL. After 24 h of incubation at 37°C with shaking, 100 µL from each treatment group was plated onto LB agar plates and incubated overnight at 37°C. Plates were then examined for visible colony formation, and the MBC was determined as the lowest concentration showing complete inhibition of bacterial growth.

Live/Dead Fluorescence Staining Assay

For live/dead flourecence staining, control cells and cells treated with AgNPs underwent staining for 20 min to distinguish between viable and dead cells. This involved using a combination of 6.0 µM SYTO 9 and 30 µM propidium iodide (PI) from the Live/Dead BacLight Viability kit (L13152, Invitrogen, Molecular Probes, Inc., Eugene, OR, USA). Following staining, fluorescence microscopic imaging of the cells was conducted using the LEICA DM 4000 B microscope, Leica Microsystems, Denmark. This imaging technique allowed for the visualization and differentiation of viable and dead cells based on their fluorescence properties. The SYTO 9 stain selectively labeled viable cells, emitting green fluorescence upon binding to nucleic acids, while the PI stain highlighted dead cells, emitting red fluorescence by penetrating damaged cell membranes.[35]

SEM Analysis of Treated Cells

SEM was employed to investigate the pronounced effects of AgNPs on individual cells. The process began by fixing both control and treated cells with 3% glutaraldehyde overnight at 4°C, ensuring the preservation of cellular structures. Subsequently, the fixed samples underwent dehydration using a series of ethanol solutions with increasing concentrations (40%, 50%, 60%, 70%, 80%, and 90%) for 15 min each, followed by absolute ethanol for 20 min.[36] This step facilitated the removal of water from the samples while maintaining cellular integrity. Once dehydrated, the samples were mounted onto SEM carbon tape and allowed to air-dry at RT. Before imaging, a thin layer of gold coating was applied to the samples to enhance their conductivity and improve imaging quality. In addition to SEM imaging, EDX and elemental mapping were conducted on AgNPs-treated cells. This analysis aimed to confirm that the observed cellular effects were specifically due to the action of AgNPs. By assessing the elemental composition of the treated cells, any potential interactions or alterations induced by AgNPs could be elucidated, providing valuable insights into their mechanism of action. These analyses aimed to provide a comprehensive understanding of the impact of generated AgNPs on bacterial viability and morphology. All antibacterial experiments, including MBC assays, fluorescence staining, and SEM imaging, were performed in biological triplicates (n = 3).

Results and Discussion

Biosynthesis of NPs Using *Bacillus subtilis* Strains

Bacterial-mediated synthesis is recognized as an environmentally friendly route and acknowledged for its ability to produce highly effective and stable NPs.[34] Bacteria serve as potent nanofactories, facilitating the production of diverse NPs types, including silver, gold, iron, zinc, copper, etc.[37–41] These NPs exhibit superior stability and efficiency, making them promising candidates for various applications such as anticancer, antibiofilm, and antimicrobial treatments.[42,43] Certain bacterial species stand out for their proficiency in generating essential biological compounds and have already been successfully industrialized to produce various products. Notable examples include *E. coli, P. putida*, and *Bacillus*

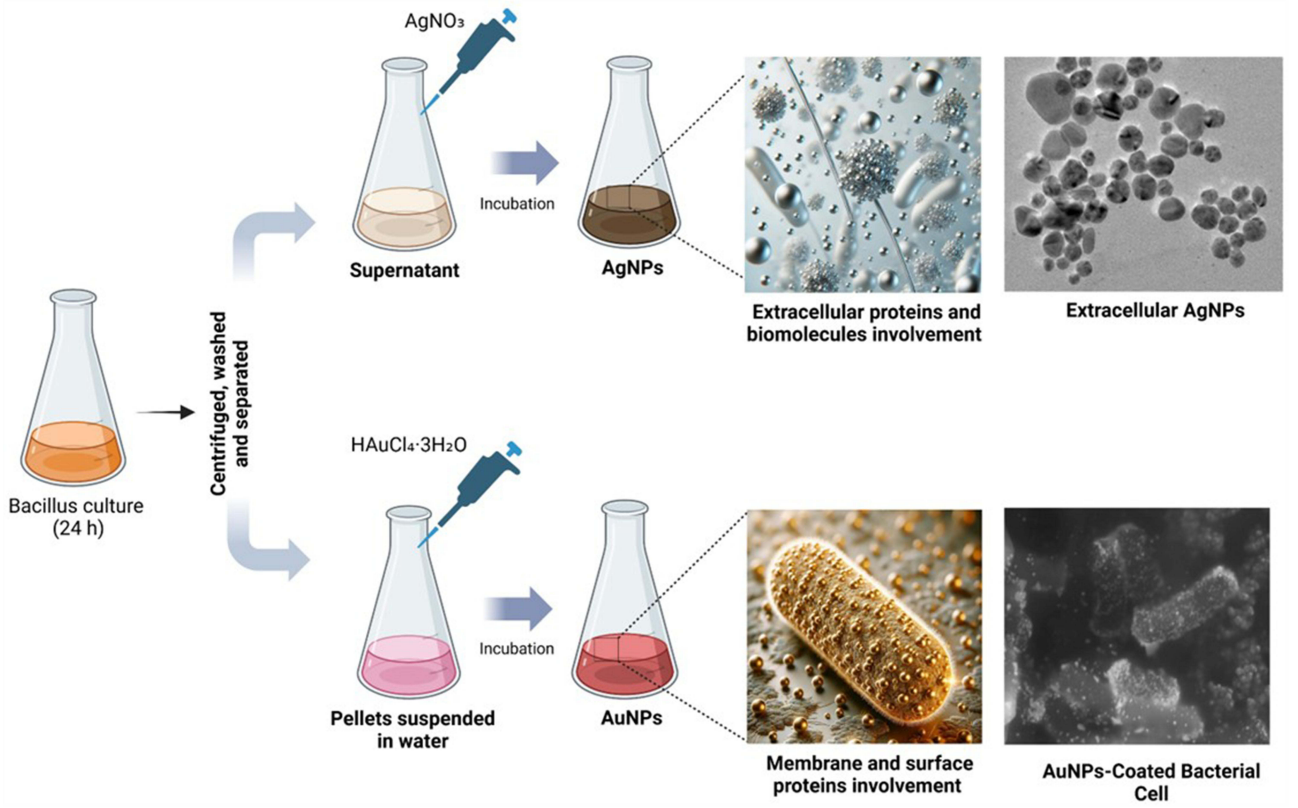

Figure 1 Biosynthesis of extracellular AgNPs and membrane-bound AuNPs by *Bacillus sp.* cultures were fractionated to obtain supernatant (extracellular proteins) and cell pellets (membrane proteins). $AgNO_3$ added to the supernatant yielded AgNPs via protein-mediated reduction; $HAuCl_4 \cdot 3H_2O$ added to resuspended pellets produced AuNPs deposited on the cell surface.

species, each renowned for their applications in different areas.[44] In our current study, we delved into the exploration of *Bacillus* species for the eco-friendly synthesis of AgNPs and AuNPs using distinct routes (Figure 1).

Results obtained from this study demonstrated that in the initial stages of NPs synthesis, both *B. subtilis* strains, B168 and B3610, exhibited proficiency in producing AgNPs. As illustrated in Figure 2, the UV-Vis peak of AgNPs production from B168 (A) and B3610 (G) is evident in unpurified samples. Subsequent images depict distinct and well-defined peaks for purified AgNPs in the 400–500 nm region for both strains, B168 (B) and B3610 (H), with visible color differences in the synthesis medium. The observed differences in optical properties strongly indicate variations in the size, shape, or concentration of the synthesized AgNPs between the two bacterial strains.[45] Significantly, B3610-AgNPs demonstrated a more robust and distinctive presence, characterized by a heightened intensity and a noticeably higher band in the UV-Vis spectrum than B168-AgNPs. This suggests that the concentration of AgNPs is higher, and the size range is narrower with B3610 than with B168. Additionally, the color of the media, which transitions to a dark brown shade, appears darker for B3610 compared to the B168 strain. This color variation corresponds to the amount, shape, and size of AgNPs produced in the synthesis medium.[46]

For AuNPs production by *B. subtilis* strains as well, distinct visual and UV-Vis spectral changes were observed. Figure 3A and F demonstrated the broad peak in UV-vis in the range of 500–600 nm, corresponding to the formation of AuNPs in the medium. B168-AuNPs exhibited a light pink color (Figure 3A), whereas B3610-AuNPs appeared much darker, nearly black (Figure 3F), reflecting differences in particle size distribution and aggregation between the strains. Upon purification, the UV–Vis spectrum of B3610-AuNPs showed a sharp and narrow plasmon peak (Figure 3G), whereas B168-AuNPs exhibited a comparatively broader peak (Figure 3B), indicating more uniform particle formation in the B3610 strain.

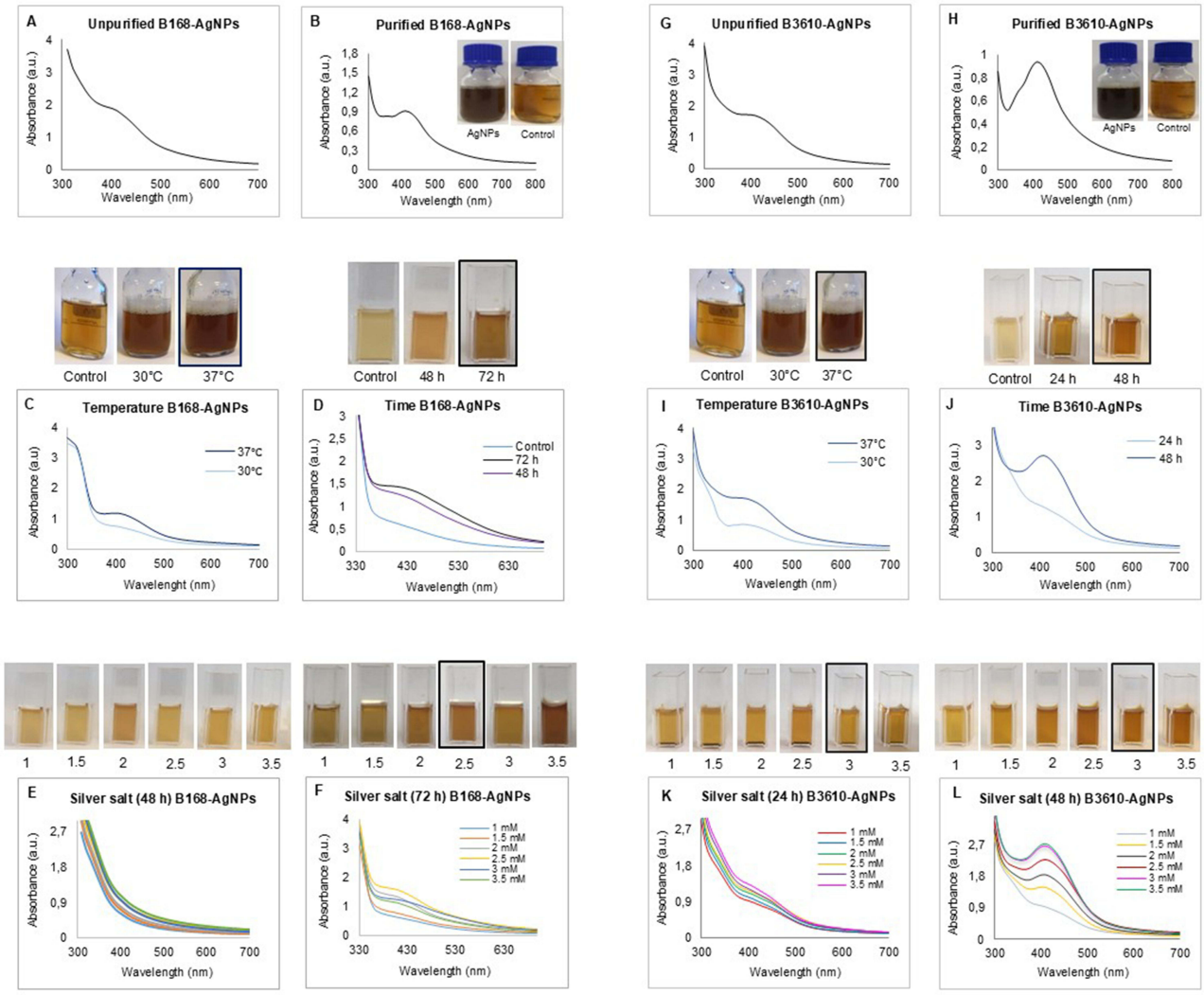

Figure 2 UV-Vis spectra and visible analysis of AgNPs formation from B168 and B3610 strains. For B168-AgNPs: (**A**) UV-Vis spectra for unpurified AgNPs, (**B**) UV-Vis spectra for purified AgNPs, (**C**) Temperature optimization for B168-AgNPs production, (**D**) Time optimization for B168-AgNPs production, (**E**) Silver salt concentration optimization for B168-AgNPs production at 48 h, and (**F**) and at 72 h. For B3610-AgNPs: (**G**) UV-Vis spectra for unpurified, (**H**) UV-Vis spectra for purified AgNPs (**I**) Temperature optimization for B3610-AgNPs production, (**J**) Time optimization for B3610-AgNPs production, (**K**) Silver salt concentration optimization for B3610-AgNPs production at 48 h, and (**L**) and at 72 h.

The observed differences in NPs synthesis efficiency between B3610 and B168 could be attributed to these bacterial strains' distinct surface properties and genetic makeup. Specifically, B168 is known to have a mutation in the comK gene, which is critical for competence development, and deletions in the srfA gene cluster, affecting surfactin production. Strain B3610, unlike B168, is known to retain more of its "wild-type" characteristics, as it has not undergone extensive domestication through laboratory culturing.[47] This retention of natural capabilities may include the ability to form complex biofilms, swarming motility, enhanced metabolic activity, production of certain enzymes, and secretion of extracellular components, all of which could contribute to more efficient NPs synthesis.[48] In addition, the presence of surfactin in B3610, absent in strain B168, may influence NPs synthesis capabilities by affecting surface properties and interactions with metal salts. Differences in swarming behavior, attributed to surfactin production, suggest broader variations in metabolic activity and genetic expression profiles, potentially impacting NPs synthesis efficiency. Further study into the role of surfactin and other factors influencing swarming behavior could elucidate mechanisms underlying differential NPs synthesis in these strains.[47] Another important factor is the presence of strain-specific surface proteins, which play a critical role in mediating interactions with metal ions during NPs synthesis. *B. subtilis* 3610 may express a distinct repertoire of surface-

https://doi.org/10.2147/IJN.S527950

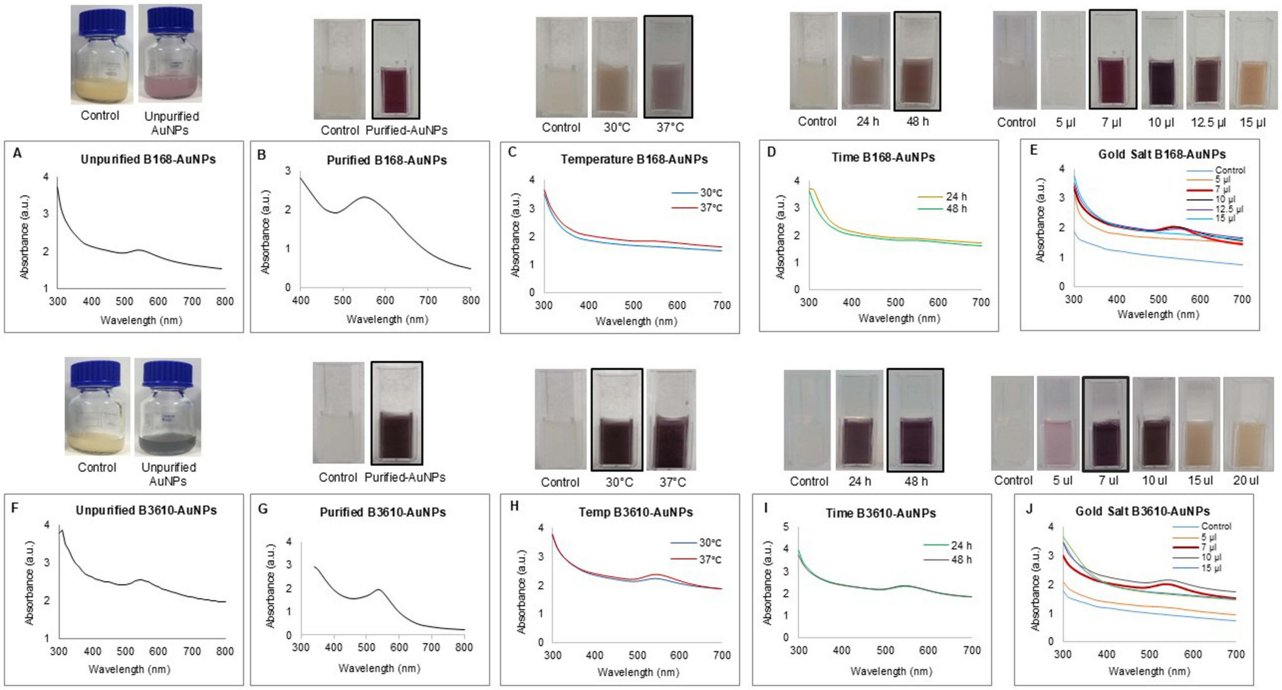

Figure 3 UV-Vis Spectra and Visible Analysis of AuNPs Formation from B168 and B3610 strains. For B168-AuNPs: (**A**) UV-Vis spectra for unpurified AuNPs, (**B**) UV-Vis spectra for purified AuNPs, (**C**) Temperature optimization, (**D**) Time optimization, (**E**) Gold salt concentration optimization. For B3610-AuNPs: (**F**) UV-Vis spectra for unpurified AuNPs, (**G**) UV-Vis spectra for purified AuNPs, (**H**) Temperature optimization, (**I**) Time optimization, (**J**) Gold salt concentration optimization.

associated proteins compared to B168, potentially leading to differences in ion binding, nucleation, and NPs growth dynamics.[49] These surface proteins may function as stabilizing agents or biological catalysts, influencing both the rate and uniformity of NPs formation. Moreover, genetic differences between B3610 and B168 may influence the expression of genes related to stress response, metal ion uptake, and NPs metabolism.[50] As a wild-type strain, *B. subtilis* 3610 is more robust in adapting to various environmental conditions, retaining traits that enable it to survive in diverse environments, including high salt concentrations and the ability to reduce them. In contrast, the mutations or genetic modifications accumulated during the laboratory domestication of *B. subtilis* 168 may have altered the expression of genes responsible for these adaptive traits, resulting in diminished capabilities compared to the more "wild-type" B3610 strain. Previously, Plaza et al reported AgNPs forming from *B. subtilis* T-1[51] and Kabirdass et al. *Bacillus* mn14, which was reported as a soil-borne pathogen.[52] Both studies reported limited information about NPs production and antibacterial applications; by comparing these strains, we demonstrated a deeper understanding.

Optimization of NPs Synthesis Conditions

The optimization studies conducted to refine the synthesis process.[53] In temperature optimization studies for AgNPs, both B168 (Figure 2C) and B3610 strains (Figure 2I) exhibited optimal NPs production at 37°C could be attributed to the temperature-dependent enzymatic activities within the bacterial cells, influencing the rate of silver ion reduction and subsequent NPs formation. B3610 strain exhibited a notably accelerated synthesis rate for the time of synthesis, reaching optimal production within 48 h, while B168 strain required 72 h to achieve comparable results (Figure 2D and J). This temporal distinction implies inherent variations in the bioreduction capabilities of the two strains or differences in their respective extracellular environments that influence the reduction kinetics of silver ions. The exploration of silver salt optimization provided valuable insights into the concentrations conducive to optimal AgNPs production. B168 strain demonstrated an optimal silver salt concentration of 2.5 mM, while B3610 strain exhibited superior performance at a slightly higher concentration of 3 mM (Figure 2E, F, K and L). This

discrepancy in optimal concentrations suggests strain-specific variations in the uptake and utilization of silver ions, shedding light on the distinct metabolic pathways or cellular mechanisms involved in the bioreduction process. These findings highlight how genetic differences, environmental conditions, and reaction kinetics influence AgNPs synthesis in *Bacillus* strains. The variations in synthesis rate, intensity, and optimal conditions point to strain-specific factors that govern NPs formation.

For AuNPs optimization studies, the distinct responses of B3610 and B168 strains to temperature variations were noted, with optimal NPs production occurring at 37°C for B168 (Figure 3C) and 30°C for B3610 strain (Figure 3H), respectively, hinting at the involvement of temperature-sensitive enzymes or metabolic pathways in the bioreduction of gold ions. For the time optimization studies, both strains revealed 48 h for NPs production as the optimum time (Figure 3D and I). Similarly, for gold salt concentration, both the strains showed 7 µL as the optimum salt for AuNPs production in the medium (Figure 3E and J). All the UV spectra results align with the color intensity of the synthesis medium highlighted in the figures. The significance of our study lies in its innovative approach towards NPs production, leveraging *Bacillus* cells' extracellular medium for the synthesis of AgNPs, while utilizing the remaining cellular pellet for intracellular synthesis of AuNPs. Notably, both extra and intracellular synthesis pathways were successfully demonstrated, positioning this methodology as a sustainable means for both types of NPs production simultaneously. In terms of purification, the process diverged for AgNPs and AuNPs. The purification of AgNPs proved straightforward, facilitated by their production in an extracellular medium devoid of cells. Simple centrifugation and subsequent washing with distilled water sufficed for purification. Conversely, AuNPs purification presented greater complexity. Additional steps, including sonication and membrane digestion, were required to extract the AuNPs fully from the cellular matrix. Subsequent washing steps and ultracentrifugation were essential to collect purified AuNPs.

Quantitative Analysis and Stability Assessment

sp-ICP-MS analysis of these NPs revealed concentrations of 0.024 µg/µL for B168-AgNPs, 0.452 µg/µL for B3610-AgNPs, 0.008 µg/µL for B168-AuNPs, and 0.001 µg/µL (first peak) and 0.08 µg/µL (second peak) for B3610-AuNPs (Figure 4). The differences in NPs concentrations corresponded with the visible and UV–Vis spectra of both AgNPs types, as shown in Figure 2. Subsequent sp-ICP-MS analysis was conducted on the same AgNPs preparations after a time-lapse of 24 to 86 h of incubation at RT to assess stability. Notably, B3610-AgNPs maintained a narrower and more consistent size distribution up to 86 h, whereas B168-AgNPs exhibited a broader distribution and reduced particle counts over the same period, indicating comparatively lower stability. For AuNPs, B168 produced a relatively uniform NPs population, while B3610 generated heterogeneous distributions with two distinct peaks, corroborating the bimodal concentration values observed by sp-ICP-MS.

The stability analysis was also conducted using UV–Vis spectroscopy, and the results aligned with the sp-ICP-MS data (Figure 5). The UV–Vis stability analysis demonstrated that the NPs remained stable over a period of 2 weeks (Figure 5A,D,G and J), exhibiting consistent spectra across all NPs types. Although both preparations remained broadly stable at RT, sp-ICP-MS revealed that B3610-AgNPs maintained narrower distributions and higher counts compared to B168-AgNPs, indicating comparatively greater stability. Medium stability analysis revealed that water was the most effective medium for maintaining NPs stability, although they also exhibited stability in LB and TSB media (Figure 5B,E,H and K). Consistent NPs sizes over time, especially in water as a stabilizing medium, highlight the significance of the suspension medium influencing NPs stability. This observation is crucial for applications where the stability of NPs is a critical factor, such as in biomedical and environmental contexts.[34] TGA further contributed to understanding the thermal stability profiles of the synthesized NPs. The analogous degradation patterns observed for both AgNPs and AuNPs, commencing after ~200°C and concluding at ~400°C, suggest shared thermal vulnerabilities (Figure 5C,F,I and L). This commonality points towards the presence of similar organic capping agents or stabilizing biomolecules on the surfaces of both types of NPs, providing a foundation for further investigations into these stabilizing agents. Notably, the TGA curves of AgNPs synthesized by strains B168 and B3610 showed slight mass loss between 150–250°C, indicating the selective degradation of certain biomolecular components.[54] This phase suggests that while some surface-bound biomolecules degrade at

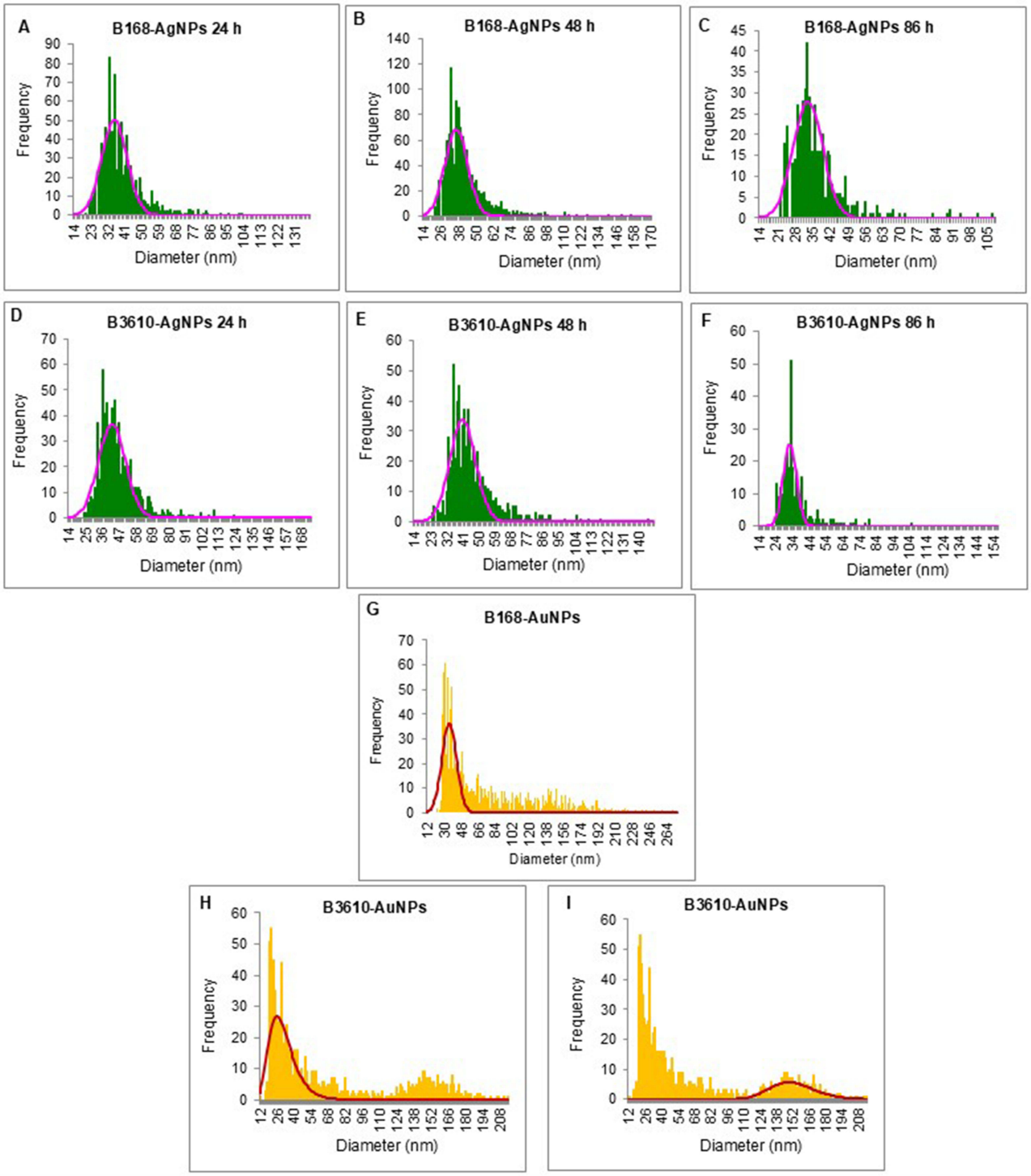

Figure 4 Sp-ICP-MS analysis of AgNPs and AuNPs from *Bacillus* strains. Sp-ICP-MS histogram of B168-AgNPs at different time intervals (**A**) after 24 h of synthesis, (**B**) after 48 h of synthesis, (**C**) after 86 h of synthesis. For B3610-AgNPs (**D**) after 24 h of synthesis, (**E**) after 48 h of synthesis, (**F**) after 86 h of synthesis. (**G**) B168-AuNPs histogram, (**H** and **I**) B3610-AuNPs histogram.

moderate temperatures, others contribute to the thermal stability of the NPs. At temperatures above 400°C, complete degradation of the biological matrix was observed, highlighting the importance of thermal thresholds when considering these biogenic NPs for high-temperature applications.

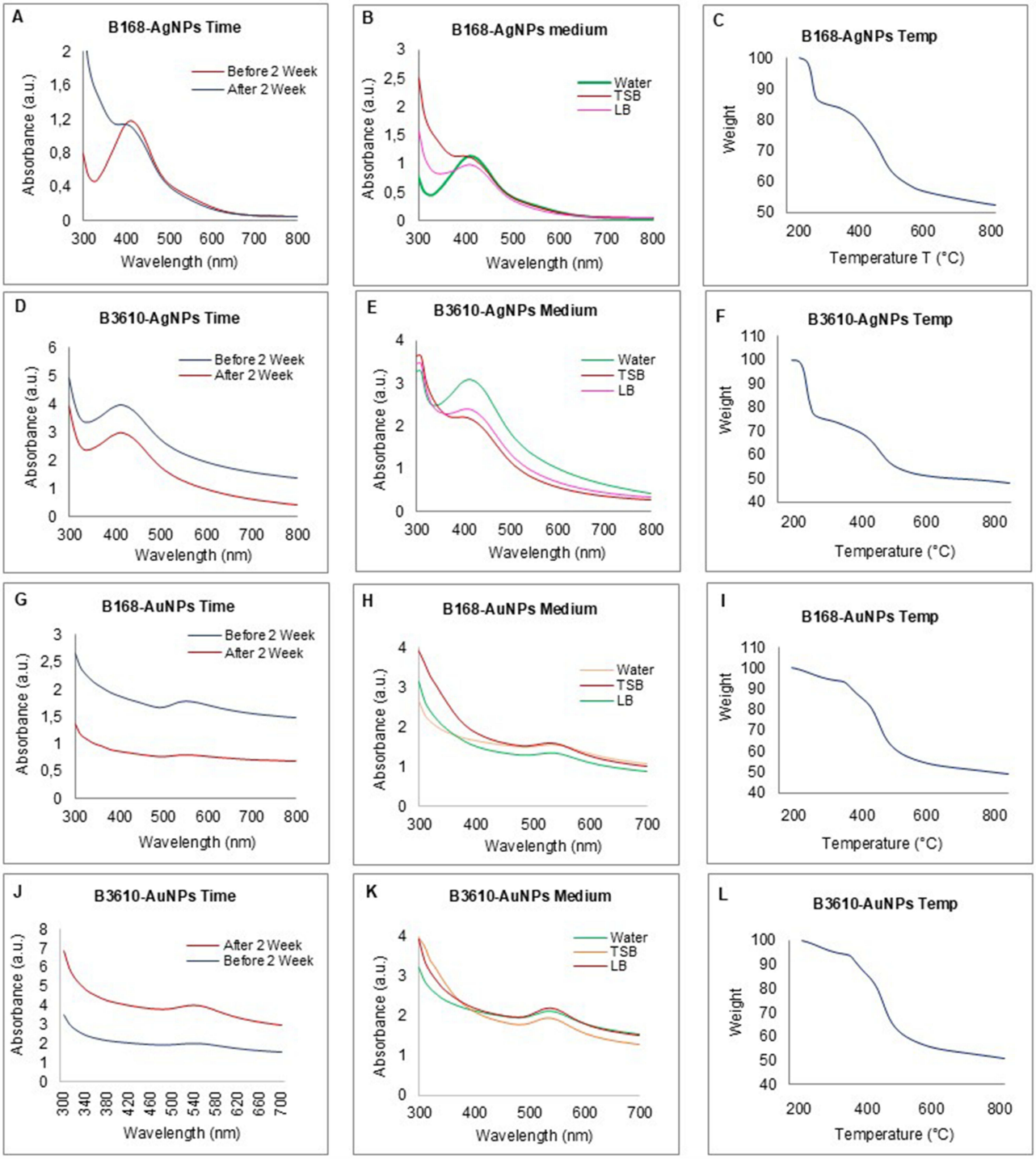

Figure 5 UV-Vis spectrum representing the stability analysis. For B168-AgNPs: (**A**) before and after two weeks of incubation at RT, (**B**) in different media (water, TSB, LB) (**C**) at the temperature range from 20–700°C measured by TGA instrument. For B3610-AgNPs: (**D**) before and after two weeks of incubation at RT, (**E**) in different media (water, TSB, LB) (**F**) at the temperature range from 20–700°C measured by TGA instrument. For B168-AuNPs: (**G**) before and after two weeks of incubation at RT, (**H**) in different media (water, TSB, LB) (**I**) at the temperature range from 20–700 °C measured by TGA instrument. For B3610-AuNPs: (**J**) before and after two weeks of incubation at RT, (**K**) in different media (water, TSB, LB) (**L**) at the temperature range from 20–700°C measured by TGA instrument.

Morphological and Elemental Characterization of NPs

Microscopic analyses employing SEM and TEM unveil the morphological intricacies of the synthesized NPs.[55] Figure 6 shows the SEM image of NPs at different resolutions for B168-AgNPs (Figure 6A–C) and B3610-AgNPs (Figure 6J–L).

https://doi.org/10.2147/IJN.S527950

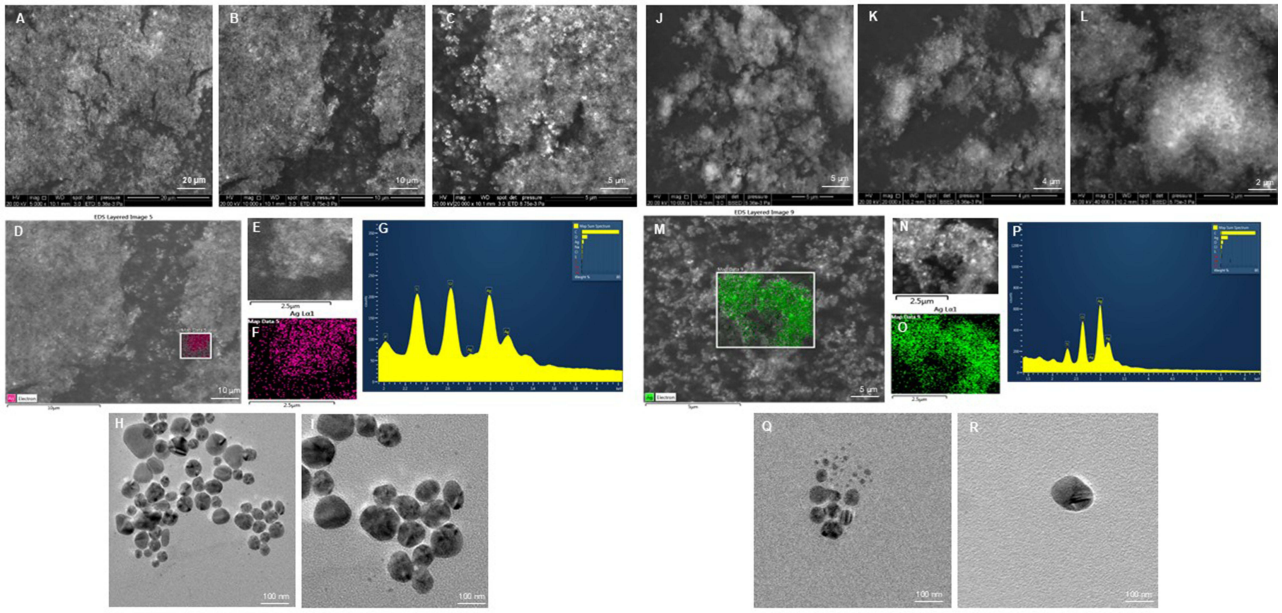

Figure 6 SEM, elemental mapping, EDX analysis of AgNPs. For B168-AgNPs, (**A**–**C**) are SEM images of AgNPs at different scales, (**D**–**F**) Elemental mapping showing a scanned image of AgNPs with silver element distribution (pink), (**G**) EDX spectrum of the elemental mapped region showing a sharp peak for silver element, (**H** and **I**) are TEM images showing spherical morphology. For B3610-AgNPs, (**J**–**L**) are SEM images of AgNPs at different scales, (**M**–**O**) Elemental mapping showing a scanned image of AgNPs with silver element distribution (green), (**P**) EDX spectrum of the elemental mapped region showing a sharp peak for silver element, (**Q** and **R**) TEM images showing spherical morphology.

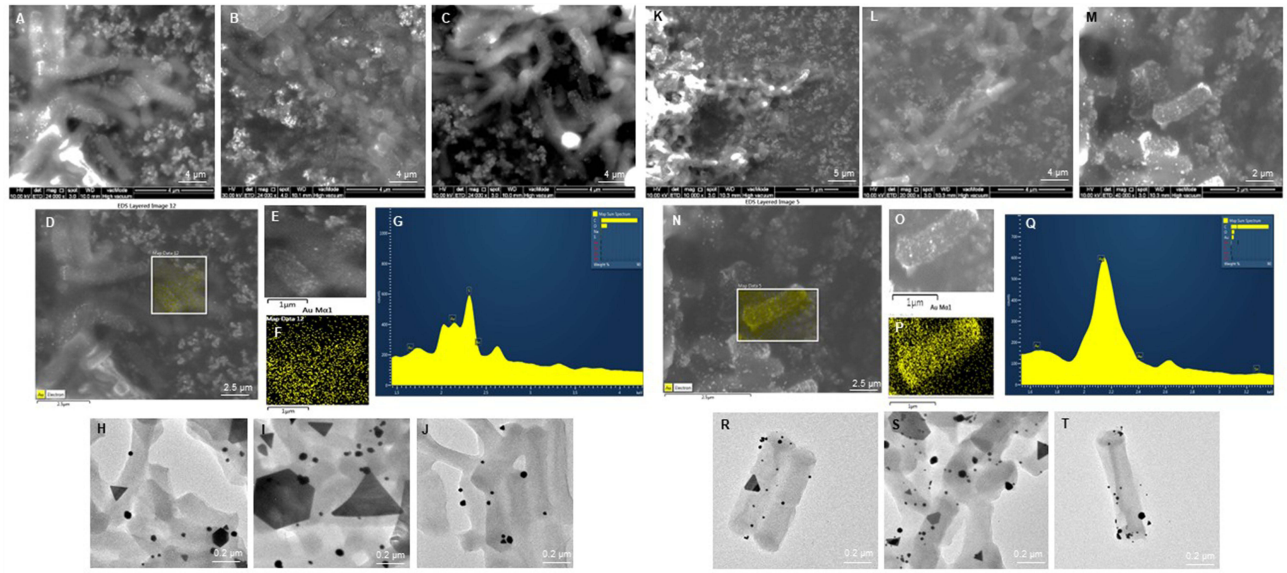

Figure 7 SEM, elemental mapping, and EDX analysis of AuNPs. For B168-AuNPs, (**A**–**C**) SEM images of AuNPs at different scales, (**D**–**F**) Elemental mapping showing a scanned image of AuNPs with gold element distribution (yellow), (**G**) EDX spectrum of the elemental mapped region showing a sharp peak for gold element, (**H**–**J**) TEM images showing particle morphology. For B3610-AuNPs, (**K**–**M**) SEM images of AuNPs at different scales, (**N**–**P**) Elemental mapping showing a scanned image of NPs with gold element distribution (yellow), (**Q**) EDX spectrum of the elemental mapped region showing a sharp peak for gold element, and (**R**–**T**) TEM images showing particle morphology.

The elemental mapping of AgNPs scanned micrograph image shows the clear distribution of silver element and respective EDX histogram from B168 with pink color (Figure 6D–G) and B3610 with green color (Figure 6M and P). As shown by TEM images of both the AgNPs, AgNPs maintain a uniform spherical morphology for B168 (Figure 6H and I) and B3610 (Figure 6Q and R). The findings demonstrate AgNPs purity and homogeneity in the samples.

For AuNPs production, the SEM images of B168-AuNPs (Figure 7A–C) and B3610-AuNPs (Figure 7K–M) showed the attachment of AuNPs on individual cells at different resolutions. It can be easily seen that the AuNPs are formed on the surface of cells and remain attached to them. An elemental mapping result indicates the AuNPs distribution over the cell surface for B168 (Figure 7D–G) and B3610 (Figure 7N–Q). The EDX spectrum showed a sharp peak for B3610 AuNPs (Figure 7Q), while the B168-AuNPs (Figure 7G) remained quite broad and showed many other elements from the cell surface, corresponding to other elements' impurities.[56] Thus, the elemental mapping further corroborates the distribution of gold on the respective NPs, offering a visual representation of their compositional heterogeneity. By further investigating the shapes of AuNPs, we received a clear and captivating array of shapes in TEM images, including triangular, spherical, and hexagonal configurations for the B168-AuNPs (Figure 7H–J). Similarly, in B3610, the AuNPs appear in triangular and spherical morphology (Figure 7R–T) and are attached to the cell membrane. The most noteworthy observation pertains to the production of AuNPs directly on the surface of microbial cells, with a subsequent attachment to the cell membrane. This phenomenon strongly suggests the active involvement of surface proteins in both the reduction and stabilization of AuNPs. Exploration of these surface proteins' identity, functionality, and abundance is warranted to elucidate this process further. In contrast, the synthesis of AgNPs presents a distinct scenario. The results indicate an entirely extracellular production of AgNPs occurring without bacterial cells. This observation points towards the pivotal role of extracellular components, such as proteins, enzymes, or other biomolecules released into the medium, in producing and stabilizing AgNPs.

Surface Chemistry Characterization

The FTIR investigation of the NPs' surface chemistry revealed multiple functional groups consistent with biomolecule involvement in reduction and stabilization (Figure 8, Table 1). Broad –OH and N–H stretching bands (~3270–3280 cm^{-1}) indicated hydrophilic groups, while aliphatic C–H stretching bands (2920–2950 cm^{-1}) corresponded to hydrophobic moieties.[57] Together, these features suggest an amphiphilic character that may influence dispersibility in aqueous and biological environments. Strong signals in the amide I (~1650–1737 cm^{-1}) and amide II (~1530 cm^{-1}) regions, along with C–N vibrations (1390–1200 cm^{-1}), confirmed the presence of proteins, highlighting their role in NPs capping and

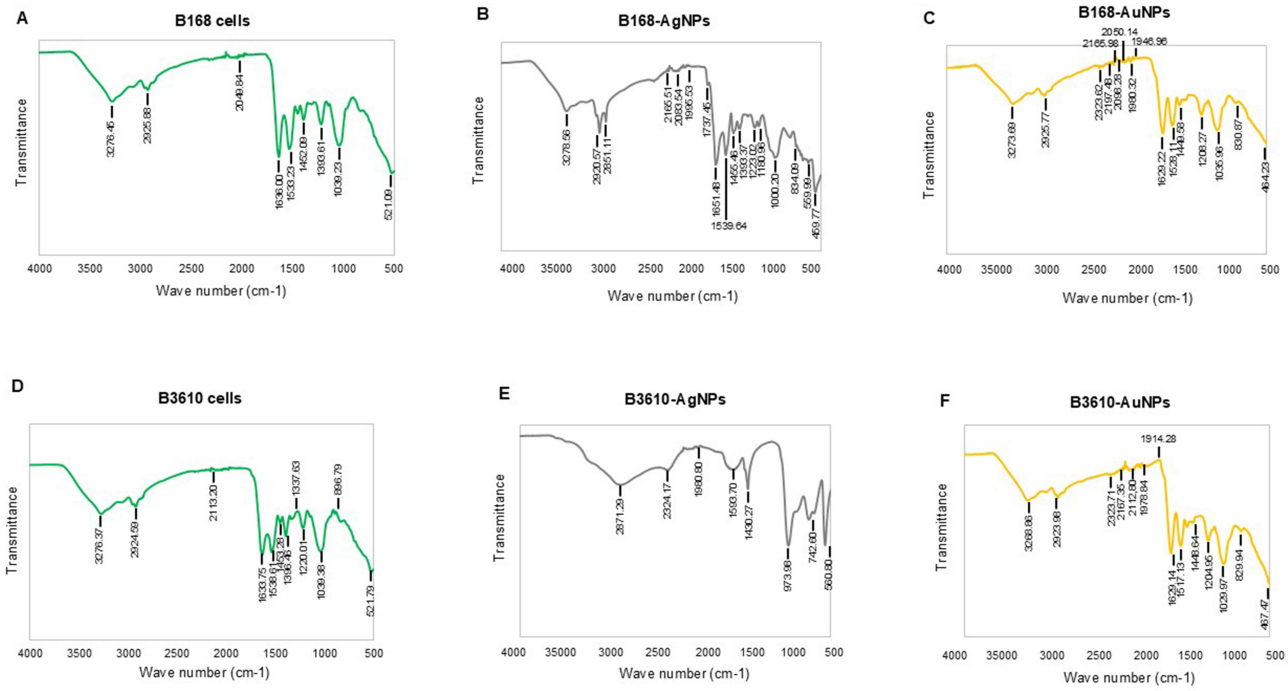

Figure 8 FTIR spectrum of (**A**) freeze-dried B168 cells (**B**) B168-AgNPs, (**C**) B168-AuNPs. (**D**) freeze-dried B3610 cells (**E**) B3610-AgNPs, and (**F**) B3610-AuNPs demonstrate the active surface groups for respective samples.

https://doi.org/10.2147/IJN.S527950

Table 1 FTIR Spectra of Cells, AgNPs, and AuNPs Synthesized by *B. Subtilis* 168 and *B. Subtilis* 3610 Reveal Both Strain- and Metal-Dependent Stabilization Patterns. For AgNPs, B168-Derived Particles Show a Distinct Lipid/Carboxyl-Associated C=O Band at 1737 cm^{-1} Along with Multiple Amide I/II and C–N Features, Consistent with a Protein- and Lipid-Rich Corona. In Contrast, B3610-AgNPs Exhibit Fewer Protein-Associated Bands but Display Strong Signals Near ~830 cm^{-1}, Indicative of Carbohydrate/Phosphate Contributions, Suggesting a Thinner but More Polysaccharide/Phosphate-Stabilized Corona. AuNPs From Both Strains are Characterized by Broader Absorptions in the 1946–2324 cm^{-1} Region, Consistent with Overtones/Combination Bands and/or Atmospheric CO_2, Rather Than Well-Defined Functional Groups. Compared with AgNPs, the AuNPs Spectra are Less Resolved and Lack Strong Amide/Carbohydrate Bands, Reflecting Weaker or More Heterogeneous Biomolecular Capping

Type of Bond	Cells Wavenumber (cm^{-1})	B168-AgNPs Wavenumber (cm^{-1})	B3610-AgNPs Wavenumber (cm^{-1})	B168-AuNPs Wavenumber (cm^{-1})	B3610-AuNPs Wavenumber (cm^{-1})
O–H stretching (phenolic, alcohols) and N–H stretching (amines, amides)	3276.45	3278.56	–	3273.69	3268.86
C–H stretching (aliphatic $–CH_3$/$–CH_2$)	2952.88	2920.57, 2851.11	2871.29	2925.77	2923.98
C≡C stretching (alkyne) / C≡N stretching (nitriles)	2049.84	2165.51, 2083.54, 1995.53	2324.17, 1980.80	2323.62, 2197.48, 2165.98, 2098.28, 2050.14, 1980.32, 1946.96	2323.71, 2167.35, 2112.80, 1978.84, 1914.28
Amide I (C=O stretching of proteins/ peptides) and/or aromatic C=C stretching	1636.00, 1533.23	1737.45, 1651.48, 1539.64	1593.70	1629.22, 1528.11	1629.14, 1517.13
CH_3, CH_2 asymmetric deformation and N–H bending (proteins)	1452.09	1455.46	1430.27	1449.58	1448.64
C–N aromatic amino groups	1393.61	1393.37, 1223.02, 1180.96	–	1208.27	1204.95
C–O stretching vibrations of amide linkages and carbohydrates (with overlapping contributions from C–N, C–O–C, and C–O–P modes)	1039.23	1000.20,	973.98	1038.96	1029.97
Aromatic C–H out-of-plane bending / phosphate group vibrations	–	834.09	742.60	830.87	829.94
C–C skeletal vibrations / possible metal–ligand vibrations	521.09	559.99, 459.77	560.80	464.23	467.47

stabilization.[58] Additionally, low-frequency bands (1000–800 cm^{-1}) indicated contributions from carbohydrates and phosphate groups, further supporting biomolecule involvement in stabilization. This molecular fingerprint elucidates the biogenic synthesis mechanism and provides a roadmap for tailoring NPs toward specific biomedical applications.[59]

MALDI-TOF spectra showed distinct biomolecular peaks associated with AgNPs surfaces, supporting stabilization by bacterial metabolites, whereas AuNPs from both strains lacked clear, consistent surface-associated signals under our acquisition settings (Figure 9). Based on these findings, and considering their ease of synthesis, purification, and higher potential for antibacterial applications, we proceeded with AgNPs as the primary focus of this study.

Zeta Potential and AFM Analysis

To further characterize these NPs, we examined their surface charge using zeta potential analysis. Interestingly, only minor differences were observed between the two strains: B168-AgNPs exhibited a zeta potential of –25.3 mV, while B3610-AgNPs showed –23.8 mV (Figure 10A and B).

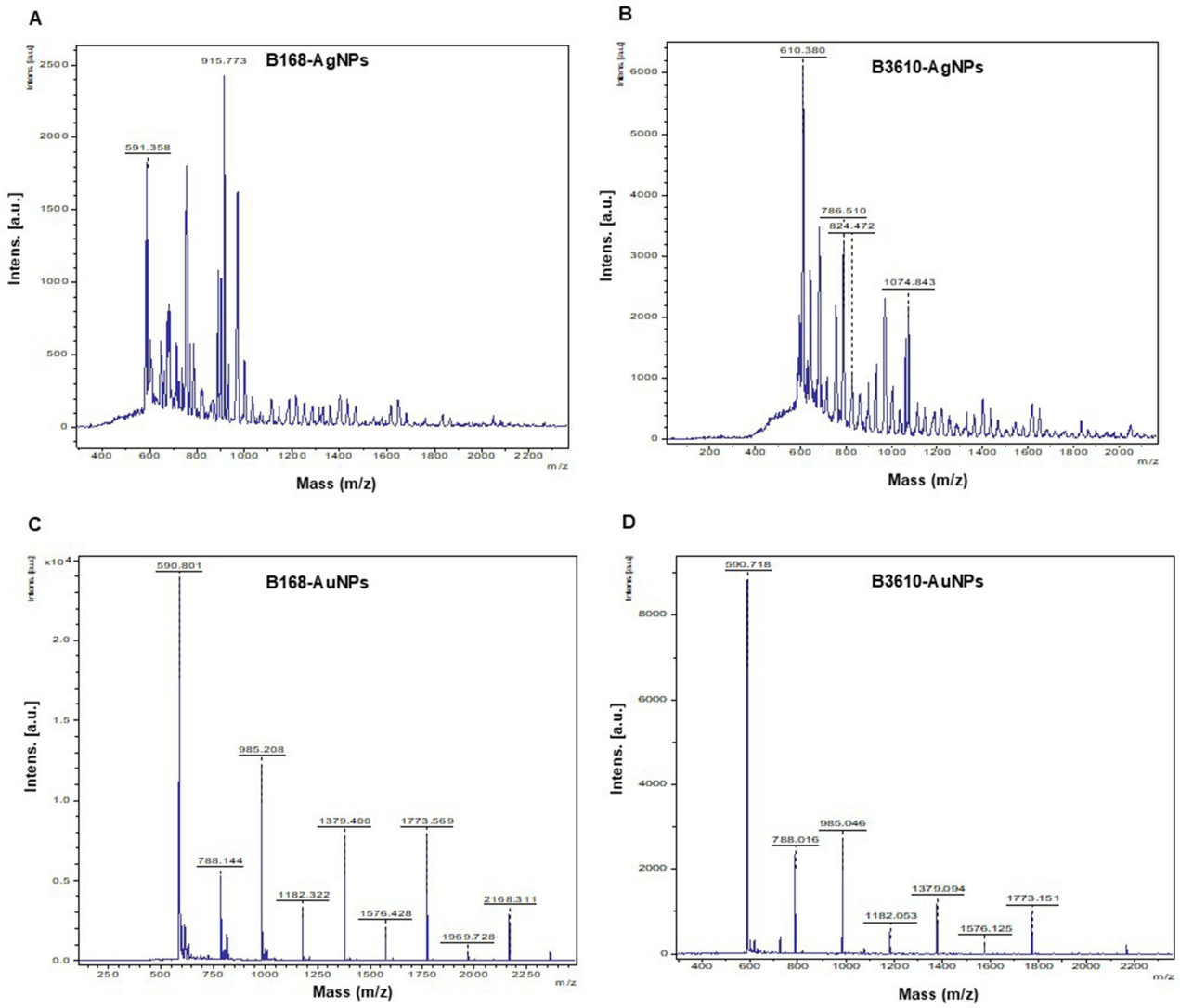

Figure 9 MALDI-TOF spectrum of (**A**) B168-AgNPs, (**B**) B3610-AgNPs, (**C**) B168-AuNPs (**D**) B3610-AuNPs.

These findings suggested that both AgNPs variants may exhibit similar antibacterial effects, which was not the case here. Hence, we dug further into AgNPs structure characteristics. We employed AFM to analyze the structural characteristics of the AgNPs.[60] Our analysis revealed a notable difference: B168-AgNPs exhibited a broader range in height, ranging from 5 to 40 nm, whereas B3610 AgNPs showed less variability, with heights predominantly falling within the range of 15 to 30 nm (Figure 10C and D). Furthermore, B168-AgNPs displayed significant aggregation, forming clusters, while B3610 AgNPs exhibited a more uniform distribution, indicating monodispersity with even spacing. Despite centrifugation and removal of cell debris, the observed aggregation in B168-AgNPs may be attributed to a thick corona layer that remains attached to the particles, along with residual extracellular components in the medium.[61] Conversely, the even size and distribution of B3610-AgNPs suggest a more controlled synthesis process. These structural differences may also contribute to variations in their antibacterial effects, which will be further elucidated in subsequent discussions. For AuNPs, due to lower yield, greater complexity in extraction, and lack of consistent uniformity in B168-AuNPs and B3610-AuNPs, we chose to exclude AuNPs from antibacterial assays. The study thus focuses on AgNPs, which were more abundant, stable, and biocompatible for our target applications.

https://doi.org/10.2147/IJN.S527950

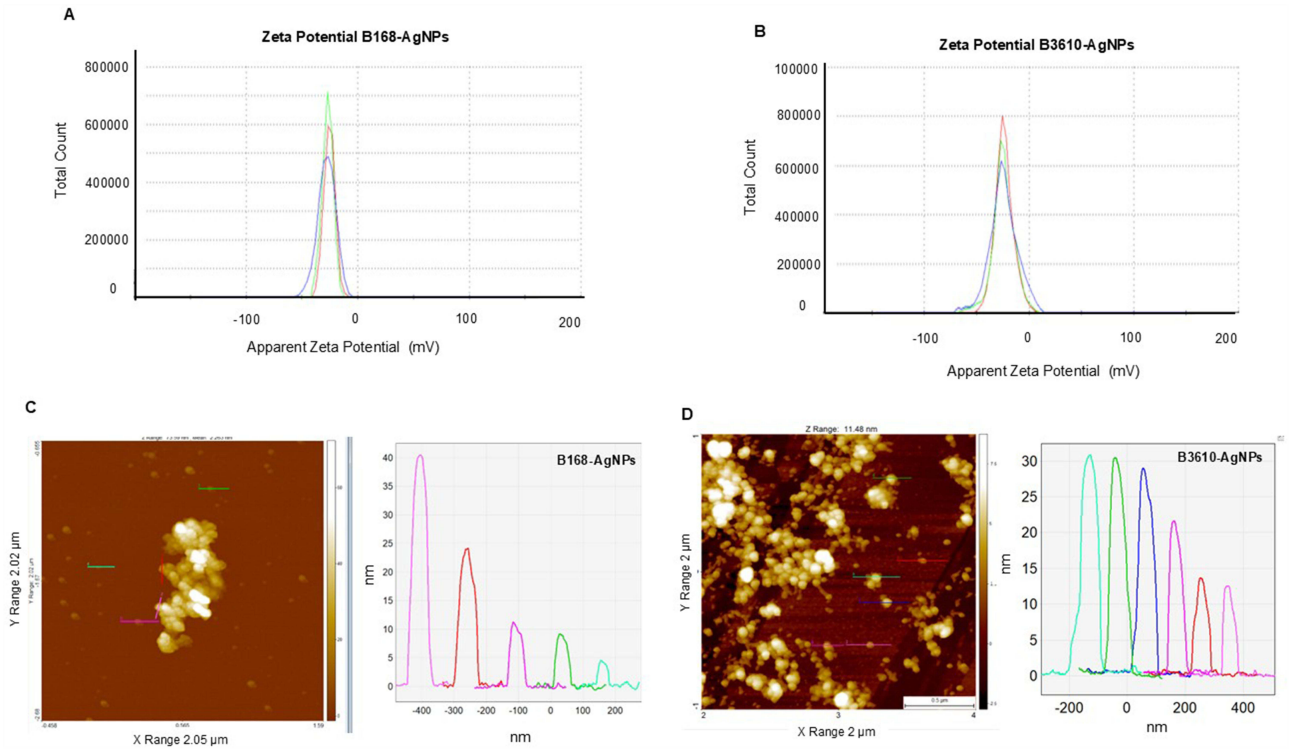

Figure 10 Zeta potential analysis of (**A**) B168-AgNPs, (**B**) B3610-AgNPs. AFM analysis of (**C**) B168-AgNPs (**D**) B3610-AgNPs.

Comparative Antibacterial Activity of AgNPs Against *P. Aeruginosa* and *E. Coli*

To evaluate the antimicrobial potential of the synthesized AgNPs, we compared their efficacy against two clinically relevant Gram-negative pathogens: *P. aeruginosa* and *E. coli*. These organisms were selected due to their global importance as multidrug-resistant bacteria, characterized by robust outer membranes and active efflux systems that limit the effectiveness of conventional antibiotics. Antibacterial activity was assessed using plate inhibition assays, live/dead fluorescence staining, and SEM to examine bacterial morphology post-treatment. The comprehensive antibacterial assessment showcased a clear distinction in the effectiveness of two AgNPs types, with B3610-AgNPs exhibiting superior efficacy compared with B168-AgNPs. The antibacterial activity was particularly noteworthy, with B3610-AgNPs demonstrating significant potency at substantially lower concentrations than their B168 counterparts. Specifically, B168-AgNPs required higher concentrations, ie, 16 µg/mL for *P. aeruginosa* (Figure 11A–G) and 32 µg/mL for *E. coli* (Figure 11H–N) to complete inhibition of respective cells, the MBC value. In comparison, B3610-AgNPs exhibited remarkably better antibacterial effects at concentrations as low as 2 µg/mL against *P. aeruginosa* (Figure 11O–T) and 8 µg/mL against *E. coli* (Figure 11U–Z). This concentration-dependent variation suggests inherent differences in the mechanisms or magnitude of antibacterial action between the two strains, emphasizing the heightened effectiveness of B3610-AgNPs in inhibiting bacterial growth. The observed stronger antibacterial effects of B3610-AgNPs compared to B168-AgNPs may be attributed to differences in the surface corona surrounding the NPs. B168-AgNPs were generally larger and carried a thicker, more complex proteinaceous corona, whereas B3610-AgNPs were smaller and coated with a thinner corona. A thicker corona layer can influence NPs toxicity by modulating adhesion to bacterial cell surfaces and limiting penetration through the membrane. FTIR data supports this interpretation: B168-AgNPs exhibited multiple peaks corresponding to surface functional groups (−OH from phenolic compounds, N−H, and C−N aromatic amino groups), whereas B3610-AgNPs showed a comparatively simpler profile with a single dominant amide peak at 1593.70 cm^{-1} (Table 1). This suggests that B168-AgNPs are coated with a richer array of extracellular proteins and biomolecules, forming a dense corona, while B3610-AgNPs possess a thinner, less complex corona, allowing closer and more efficient interactions with bacterial membranes.

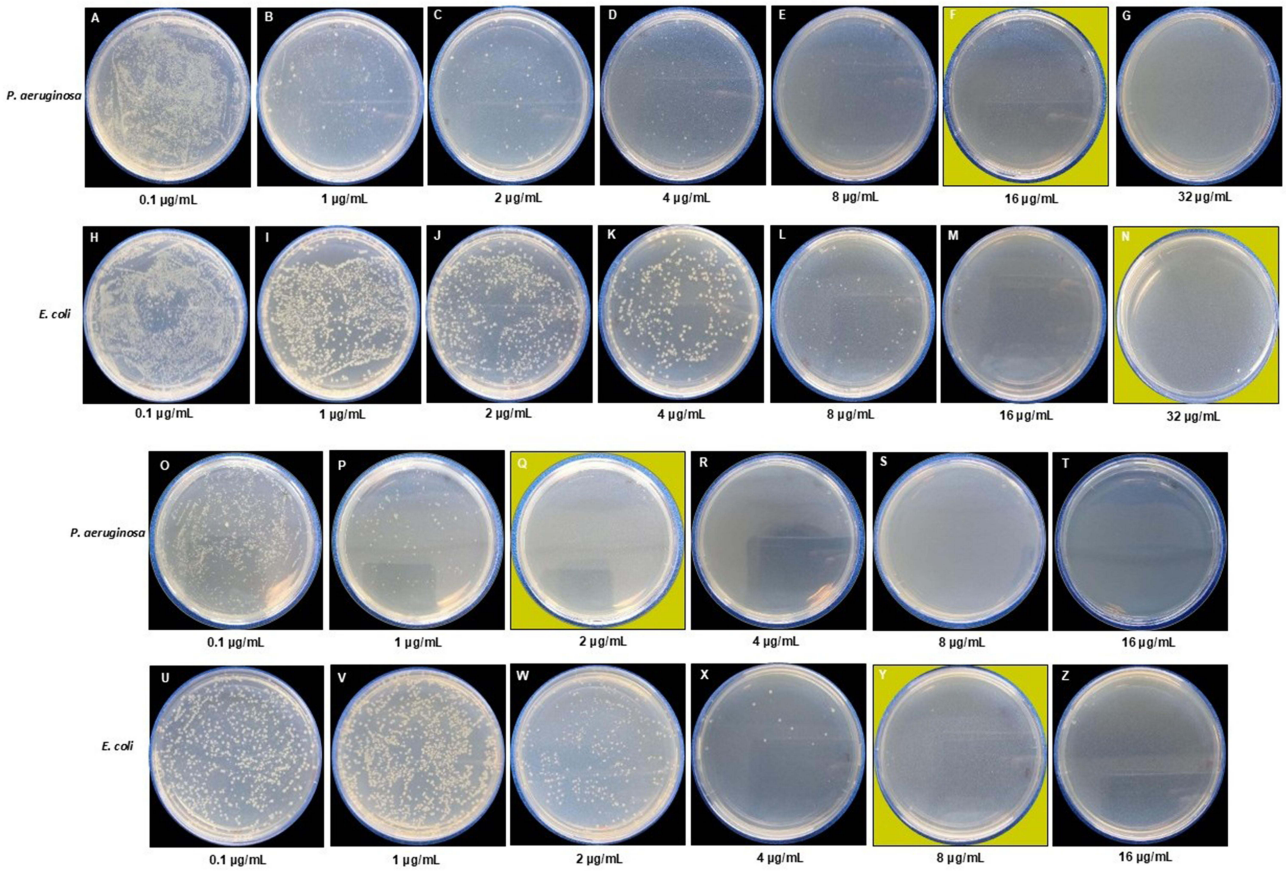

Figure 11 Cell viability test at different concentrations ranging from 0.1–32 µg/mL of (**A**–**G**) B168-AgNPs against *P. aeruginosa* and (**H**–**N**) against *E. coli*. The yellowish background shows the MBC values of respective pathogens with complete growth inhibition. (**O**–**T**) B3610-AgNPs against *P. aeruginosa* and (**U**–**Z**) against *E. coli*. Data represent one of three independent replicates.

It can be argued that NPs with a thicker corona layer may enhance antibacterial activity by facilitating uptake and disrupting cellular functions. However, in our study the smaller size and thinner corona of B3610-AgNPs enabled more efficient bacterial interactions, ultimately explaining their superior efficacy. Additionally, the composition of the corona layer, including proteins and other biomolecules, may differ between B168 and B3610 AgNPs, further influencing NPs-cell interactions and antibacterial activity.[47,48] Strain B3610 is known to have a more robust and diverse enzymatic machinery compared to B168, which may include enzymes involved in metal ion reduction, such as those encoded by the *nirB, nfrA*, and *ywjH* genes. These enzymes are critical in reducing metal ions to form NPs and could be more abundant or active in B3610, leading to faster synthesis and more stable NPs formation. Moreover, the *srfA* gene cluster, which is involved in surfactin production, differs between the two strains, potentially influencing the composition of the corona layer and the NP's interaction with bacterial membranes.[62] The genetic differences between B168 and B3610 likely play a significant role here.[63,64] For instance, the *comK* gene, which is mutated in B168, affects competence development and could indirectly influence NPs formation by altering the cell's metabolic state and secretome.[65] As a result, the NPs synthesized by these strains exhibit different sizes, shapes, and capping layers, with B3610-AgNPs showing a more effective antibacterial profile due to a thinner and more functionally active corona layer. Further research is warranted to elucidate the specific roles of these genes and others in determining the NPs synthesis pathways and the characteristics of the corona layer. Understanding these genetic influences could enable the design of NPs with tailored properties for enhanced biomedical applications.

The validity of these findings was further substantiated through live and dead staining, a technique that offers visual insights into bacterial viability (Figure 12). The staining results aligned with the quantitative antibacterial assays,

 https://doi.org/10.2147/IJN.S527950

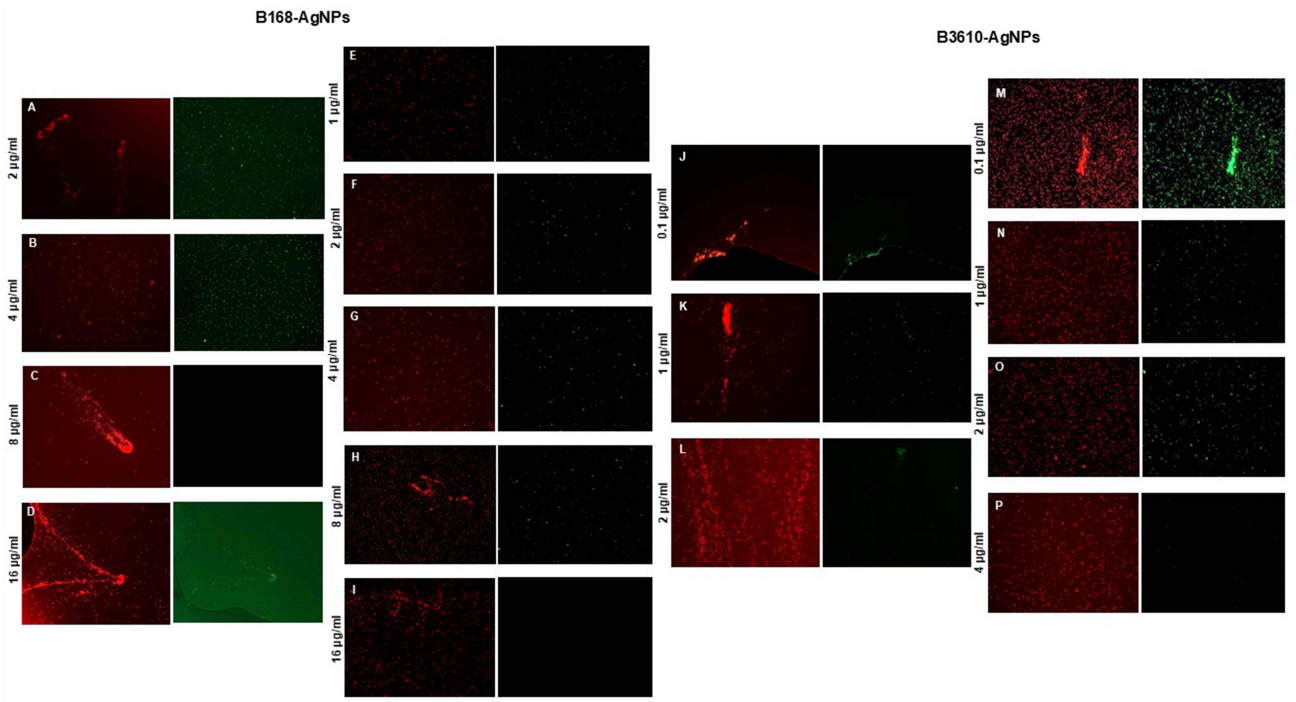

Figure 12 Live and dead staining of B168-AgNPs against (**A**–**D**) *P. aeruginosa* and (**E**–**I**) *E. coli*. B3610-AgNPs against (**J**–**L**) *P. aeruginosa* and (**M**–**P**) *E. coli*. Data represents one of three independent replicates.

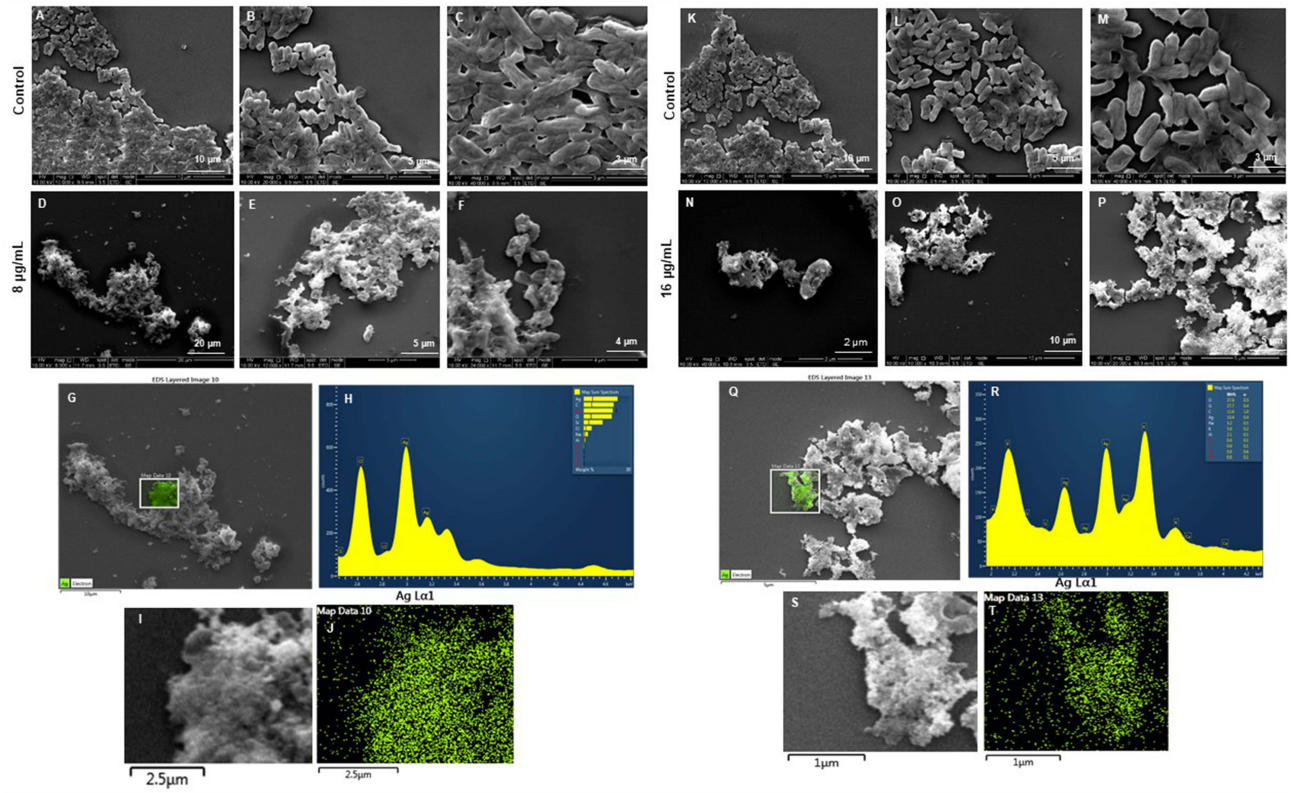

Figure 13 SEM analysis of *P. aeruginosa* cells after treatment with B168-AgNPs at two concentrations 8 and 16 µg/mL. (**A**–**C**)** Control, (**D**–**F**) B168-AgNPs treated cells with 8 µg/mL at different scales. (**G**) Scanned image of treated cells. (**H**) EDX spectrum of the chosen area showing a peak for silver element. (**I** and **J**) elemental mapping of the selected area showing silver elements in the treated cells. (**K**–**M**)** Control, (**N**–**P**) cells treated with 16 µg/mL of B168-AgNPs at different scales. (**Q**) SEM scanned image of treated cells, (**R**) EDX spectrum of the chosen area showing peak for silver element, (**S** and **T**) elemental mapping of the selected area showing silver elements in the treated cells. Data represent one of three independent replicates.

confirming the superior efficacy of B3610-AgNPs in causing bacterial cell death at lower concentrations. The absence of live (green-stained) cells in the treated samples corroborates the potent antimicrobial impact of B3610-AgNPs.

Mechanistic Insights into Structural Damage and Elemental Mapping

Structural analyses using SEM, EDX, and elemental mapping provided detailed visual evidence of the AgNPs' effects on treated pathogens.[32] The SEM images depicted discernible damage, morphological alterations, and membrane disruption in bacterial cells treated with AgNPs from the B168 strain against *P. aeruginosa* at 8 µg/mL (Figure 13A–13F) and 16 µg/mL (Figure 13K–13P).

The same AgNPs showed damage effects at 16 µg/mL (Figure 14A–F) and 32 µg/mL (Figure 14K–P) against *E. coli*, indicating the AgNPs' profound impact on the bacterial cells' structural integrity. The images are easily comparable, where one can see the intact cells without any membrane damage in control cells. In contrast, the B168-AgNPs-treated cells appeared completely shrunken, ruptured, and collapsed, with extensive NPs coverage. We further analyzed these cells with elemental mapping by scanning a micrograph of a treated cell, and the results showed the clear distribution of silver element only in that section. Hence, the damage is caused by silver ions, which must have been released from AgNPs (Figure 13G–J and 13Q–T). For *E coli* cells, a clear difference between the treated and control cells can be visualized in Figure 14. The distribution of silver elements on the *E. coli* cells reflects the cause of damage at the concentration of 16 µg/mL, highlighted with green color (Figure 14G–J), and 32 µg/mL, highlighted with pink color (Figure 14K–P). In addition, the EDX graph also represents the highest peak for silver element distribution in the affected area (Figure 14H and R).

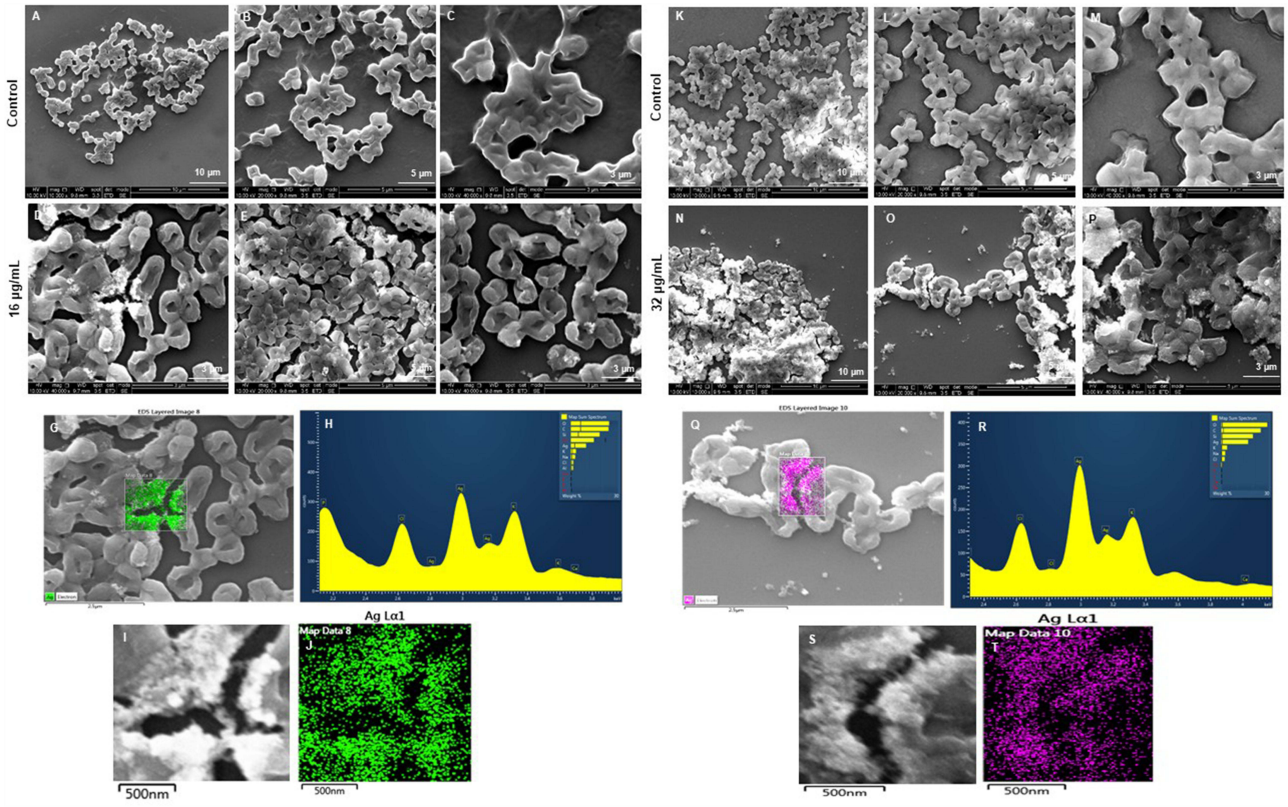

Figure 14 SEM analysis of *E. coli* cells after treatment with B168-AgNPs at two different concentrations 16 and 32 µg/mL. (**A–C**)** Control, (**D–F**) B168-AgNPs treated cells with 16 µg/mL at different scales. (**G**) Scanned image of treated cells, (**H**) EDX spectrum of the chosen area-showing peak for silver element. (**I** and **J**) elemental mapping of the selected area showing silver elements in the treated cells. (**K–M**)** Control, (**N–P**) B168-AgNPs cells treated with 32 µg/mL at different scales. (**Q**) SEM scanned image of treated cells, (**R**) EDX spectrum of the chosen area showing peak for silver element, (**S** and **T**) elemental mapping of the selected area showing silver elements in the treated cells. Data represent one of three independent replicates.

https://doi.org/10.2147/IJN.S527950

The superior antimicrobial efficacy of B3610-AgNPs is particularly noteworthy, demonstrating substantial damage at remarkably lower concentrations of 2 µg/mL against *P. aeruginosa* (Figure 15) and 8 µg/mL against *E coli* (Figure 16) compared to B168-AgNPs. The open cellular membrane structures, depicted in (Figures 15 and 16), clearly show the damaged membranes and AgNPs deposition on them, whereas the control cells appeared intact. These findings are consistent with previously published observations, where 100 ppm AgNPs induced significant morphological disruptions in both Gram-negative (*E. coli, P. aeruginosa*) and Gram-positive (*S. aureus, S. epidermidis*) bacteria over 3–-24 h exposure times.[66] In that study, untreated bacteria maintained smooth, intact surfaces, whereas treated cells appeared distorted, with leakage and fragmentation similar to the damaged membranes and silver accumulation shown in our elemental mapping and EDX results. Notably, our study demonstrates comparable effects at much lower AgNPs concentrations, emphasizing the higher potency and efficacy of the green B3610-derived AgNPs.[66] Similarly, another study reported hole formation, cell lysis in *S. aureus*, and serrated membrane deformation in *P. aeruginosa* following AgNPs treatment.[67] This heightened sensitivity not only underscores the potent bactericidal potential of B3610-AgNPs but also positions them as promising candidates for combating bacterial infections with enhanced efficiency. In addition, the EDX analysis provided evidence of silver presence within the treated bacterial cells by showing the highest peaks, indicating a direct interaction between AgNPs and microbial structures.[68] Elemental mapping further illuminated the selective accumulation of silver within the damaged regions of bacterial cells, implying a targeted mode of action.[69] This selective deposition suggests a potential interference with vital cellular components, prompting a need for detailed investigations into the specific molecular pathways affected. Moreover, achieving potent antimicrobial effects at lower concentrations not only addresses concerns related to cytotoxicity but also enhances the cost-effectiveness and practicality of employing B3610 AgNPs as antimicrobial agents.[70,71]

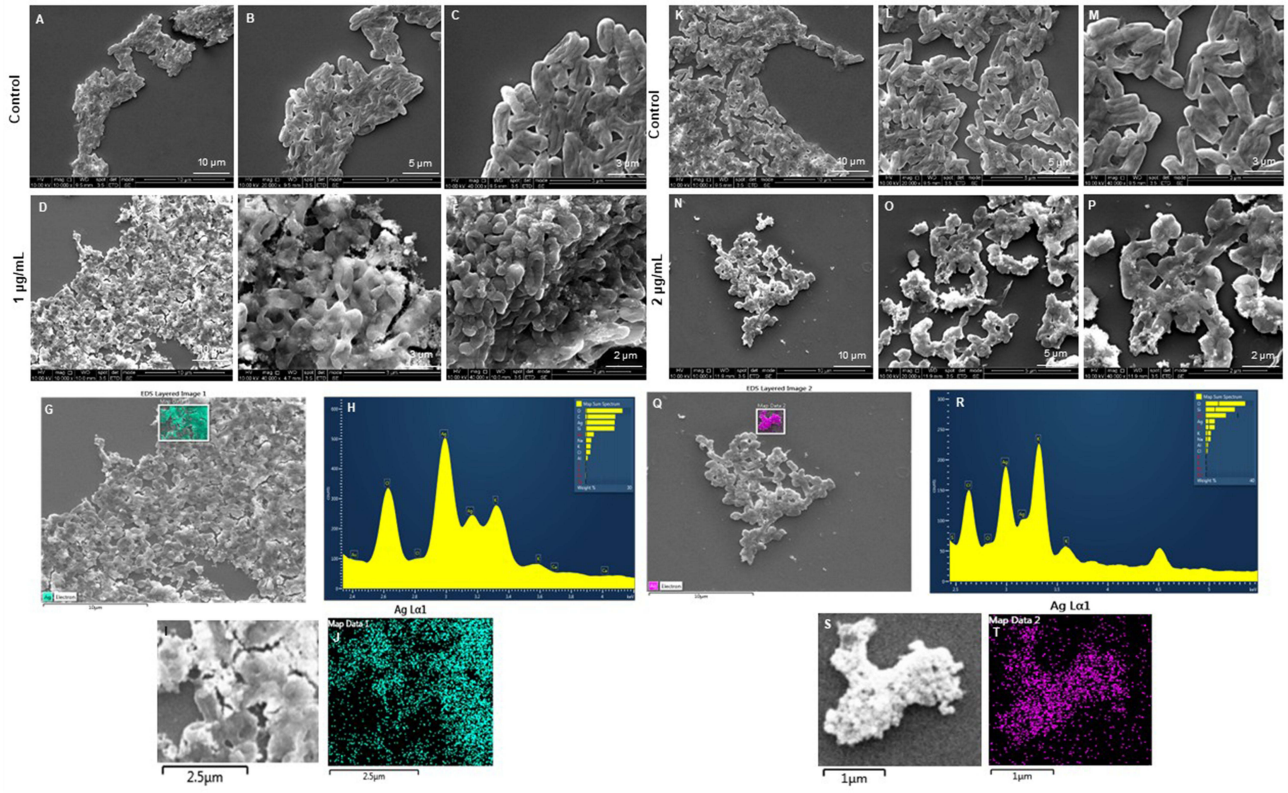

Figure 15 SEM analysis of *P. aeruginosa* cells after treatment with B3610-AgNPs at two concentrations 1 and 2 µg/mL. (**A**–**C**)** Control, (**D**–**F**) B3610-AgNPs treated cells with 1 µg/mL at different scales. (**G**) Scanned image of treated cells, (**H**) EDX spectrum of the chosen area-showing peak for silver element. (**I** and **J**) elemental mapping of the selected area showing silver elements in the treated cells. (**K**–**M**)** Control (**N**–**P**) cells treated with 2 µg/mL of B3610-AgNPs at different scales. (**Q**) SEM scanned image of treated cells, (**R**) EDX spectrum of the chosen area showing peak for silver element, (**S** and **T**) elemental mapping of the selected area showing silver elements in the treated cells. Data represent one of three independent replicates.

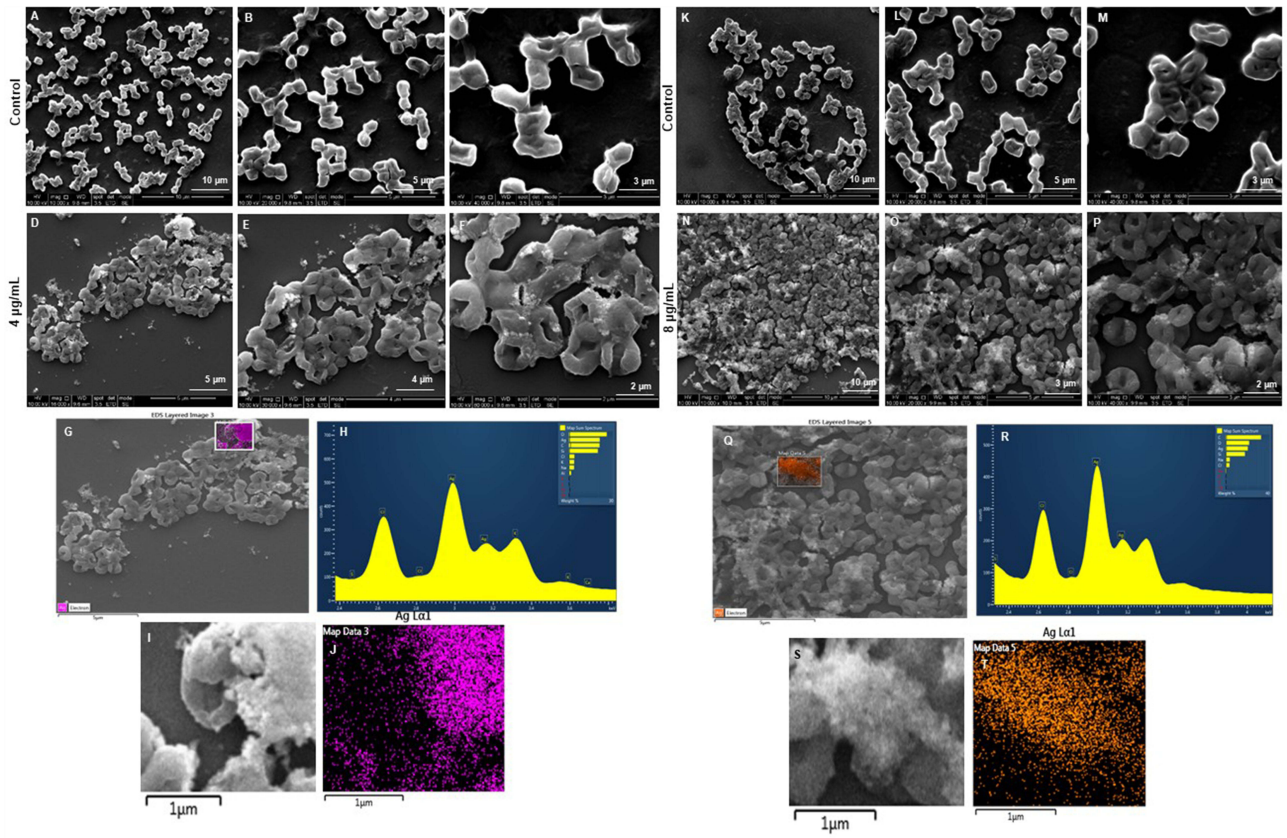

Figure 16 SEM analysis of *E. coli* cells after treatment with B3610-AgNPs at two concentrations 4 and 8 µg/mL. (**A**–**C**)** Control (**D**–**F**) B3610-AgNPs treated cells with 4 µg/mL at different scales. (**G**) Scanned image of treated cells. (**H**) EDX spectrum of the chosen area showing a peak for silver element. (**I** and **J**) elemental mapping of the selected area showing silver elements in the treated cells. (**K**–**M**)** Control, (**N**–**P**) cells treated with 8 µg/mL of B3610-AgNPs at different scales. (**Q**) SEM scanned image of treated cells, (**R**) EDX spectrum of the chosen area showing peak for silver element, (**S** and **T**) elemental mapping of the selected area showing silver elements in the treated cells. Data represent one of three independent replicates. **The untreated control cells shown in Figures 13–16 were imaged during the same experimental sessions as control samples reported previously.[16,30,35,46,54] However, distinct non-overlapping images have been selected here to serve as directly comparable references for the current study.

In addition, B3610-derived AgNPs demonstrated superior antibacterial performance compared to commercially available counterparts. For instance, Liao et al showed an MBC range of 2.813–5.625 µg/mL against *P. aeruginosa* by using a ready-to-use AgNPs stock solution (containing 1,000 µg/mL nano silver) provided by Hunan Anson Biotechnology Co., Ltd. (Changsha, China).[72] In contrast, complete inhibition of *P. aeruginosa* in our study was achieved at just 2 µg/mL. Similar findings were reported by Yuan et al, who also observed a 2 µg/mL MBC against *P. aeruginosa*.[73] These results highlight the strong antibacterial activity, high stability, and likely monodispersity of B3610-AgNPs. The observed concentration-dependent effects and bacterial membrane disruption further support their effectiveness. Such characteristics point toward the potential utility of B3610-AgNPs in developing efficient antimicrobial formulations. Continued investigation into their molecular interactions with bacterial cells will help elucidate the mechanisms underlying their activity and support their translation into biomedical applications.

Conclusions

This study shows that two closely related *Bacillus subtilis* strains produce green NPs with distinct characteristics due to genetic and phenotypic differences. The wild-type strain B3610 generated higher yields of AgNPs with greater stability and stronger antibacterial activity than the domesticated laboratory strain B168. These differences are linked to B3610's preserved traits, such as surfactin production and a broader enzymatic repertoire, which support efficient metal reduction and a thinner, carbohydrate/phosphate-rich corona. In contrast, B168 produced larger, more aggregated particles with a protein-dense corona and reduced activity. The findings highlight the importance of strain selection for microbial

nanotechnology and demonstrate that B3610-AgNPs are effective against multidrug-resistant pathogens at low concentrations, underscoring their potential for biomedical use.

Funding

Lundbeckfonden to P.S. (R303-2018-3499), NNF Grant number: NNF20CC0035580, DFF, Thematic research-Independent green research (2023): 3164-00026A, and the NordForsk (project number 105121) to I.M.

Disclosure

The authors declare no competing interests.

References

1. Singh P, Pandit S, Balusamy SR, et al. Advanced nanomaterials for cancer therapy: gold, silver, and iron oxide nanoparticles in oncological applications. *Adv Healthc Mater*. 2025;14:e2403059. doi:10.1002/adhm.202403059
2. Mellor RD, Uchegbu IF. Ultrasmall-in-nano: why size matters. *Nanomaterials*. 2022;12:2476. doi:10.3390/nano12142476
3. Balusamy SR, Joshi AS, Perumalsamy H, Mijakovic I, Singh P. Advancing sustainable agriculture: a critical review of smart and eco-friendly nanomaterial applications. *J Nanobiotechnol*. 2023;21:372. doi:10.1186/s12951-023-02135-3
4. Singh P, Garg A, Pandit S, Mokkapati VRSS, Mijakovic I. Antimicrobial effects of biogenic nanoparticles. *Nanomaterials*. 2018;8:1009. doi:10.3390/nano8121009
5. Singh P, Mijakovic I. Advances in gold nanoparticle technology as a tool for diagnostics and treatment of cancer. *Expert Rev Mol Diagnostics*. 2021;21:627–630. doi:10.1080/14737159.2021.1933447
6. Sibuyi NRS, Moabelo KL, Fadaka AO, et al. Multifunctional gold nanoparticles for improved diagnostic and therapeutic applications: a review. *Nanoscale Res Lett*. 2021;16:174. doi:10.1186/s11671-021-03632-w
7. Singh P, Pandit S, Beshay M, et al. Anti-biofilm effects of gold and silver nanoparticles synthesized by the Rhodiola rosea rhizome extracts. *Artif Cells Nanomed Biotechnol*. 2018;46:S886–S899. doi:10.1080/21691401.2018.1518909
8. Huang Y, Guo X, Wu Y, et al. Nanotechnology's frontier in combatting infectious and inflammatory diseases: prevention and treatment. *Signal Transduct Target Ther*. 2024;9(34).
9. Yang Y, Zheng X, Chen L, et al. Multifunctional gold nanoparticles in cancer diagnosis and treatment. *Int J Nanomed*. 2022;17:2041–2067. doi:10.2147/IJN.S355142
10. Singh P, Pandit S, Mokkapati VRSS, et al. Gold nanoparticles in diagnostics and therapeutics for human cancer. *Int J Mol Sci*. 2018;19:1979. doi:10.3390/ijms19071979
11. Sati A, Mali SN, Samdani N, et al. From past to present: gold nanoparticles (AuNPs) in daily life–synthesis mechanisms, influencing factors, characterization, toxicity, and emerging applications in biomedicine, nanoelectronics, and materials science. *ACS Omega*. 2025;10:33999–34087. doi:10.1021/acsomega.5c03162
12. Kouri MA, Tsaroucha A, Axakali T-M, et al. Targeting cancer cell fate: apoptosis, autophagy, and gold nanoparticles in treatment strategies. *Curr Issues Mol Biol*. 2025;47:460. doi:10.3390/cimb47060460
13. Karthikeyan C, Jayaramudu T, Núñez D, et al. Hybrid nanomaterial composed of chitosan, curcumin, ZnO and TiO(2) for antibacterial therapies. *Int J Biol Macromol*. 2023;242:124814. doi:10.1016/j.ijbiomac.2023.124814
14. Gholami-Shabani M, Sotoodehnejadnematalahi F, Shams-Ghahfarokhi M, Eslamifar A, Razzaghi-Abyaneh M. Physicochemical properties, anticancer and antimicrobial activities of metallic nanoparticles green synthesized by Aspergillus kambarensis. *IET Nanobiotechnol*. 2022;16:1–13. doi:10.1049/nbt2.12070
15. Baig N, Kammakakam I, Falath W. Nanomaterials: a review of synthesis methods, properties, recent progress, and challenges. *Mater Adv*. 2021;2:1821–1871.
16. Singh P, Mijakovic I. Green synthesis and antibacterial applications of gold and silver nanoparticles from Ligustrum vulgare berries. *Sci Rep*. 2022;12:7902. doi:10.1038/s41598-022-11811-7
17. Singh P, Kim Y-J, Zhang D, Yang D-C. Biological synthesis of nanoparticles from plants and microorganisms. *Trends Biotechnol*. 2016;34:588–599. doi:10.1016/j.tibtech.2016.02.006
18. Alharbi NS, Alsubhi NS, Felimban AI. Green synthesis of silver nanoparticles using medicinal plants: characterization and application. *J Radiat Res Appl Sci*. 2022;15:109–124. doi:10.1016/j.jrras.2022.06.012
19. Vijayaram S, Razafindralambo H, Sun YZ, et al. Applications of green synthesized metal nanoparticles - a review. *Biol Trace Elem Res*. 2023;1–27.
20. Soliman MKY, Salem SS, Abu-Elghait M, Azab MS. Biosynthesis of silver and gold nanoparticles and their efficacy towards antibacterial, antibiofilm, cytotoxicity, and antioxidant activities. *Appl Biochem Biotechnol*. 2023;195:1158–1183. doi:10.1007/s12010-022-04199-7
21. Prajapati VS, Mehta VN, Patel SK. Media formulation using statistical methodology to enhance alpha-amylase production for green synthesis of Au-NPs by Bacillus subtilis VSP4 under solid-state fermentation. *Front Bioeng Biotechnol*. 2025;13:1569902. doi:10.3389/fbioe.2025.1569902
22. Haji SH, Ali FA, Aka STH. Synergistic antibacterial activity of silver nanoparticles biosynthesized by carbapenem-resistant Gram-negative bacilli. *Sci Rep*. 2022;12:15254. doi:10.1038/s41598-022-19698-0
23. Antimicrobial Resistance C. Global burden of bacterial antimicrobial resistance in 2019: a systematic analysis. *Lancet*. 2022;399:629–655. doi:10.1016/S0140-6736(21)02724-0
24. Mills JP, Marchaim D. Multidrug-resistant gram-negative bacteria: infection prevention and control update. *Infect Dis Clin North Am*. 2021;35:969–994. doi:10.1016/j.idc.2021.08.001
25. Tawiah PO, Gaessler LF, Anderson GM, Oladokun EP, Dahl JU. A novel silver-ruthenium-based antimicrobial kills gram-negative bacteria through oxidative stress-induced macromolecular damage. *mSphere*. 2025;10:e0001725. doi:10.1128/msphere.00017-25

26. Carvalho-Silva JM, Dos Reis AC. Systematic review of silver and vanadium-based antibiofilm agents: mechanisms and efficacy in oral biofilms. *Future Microbiol*. 2025;20:639–655. doi:10.1080/17460913.2025.2520080
27. Joshi AS, Singh P, Mijakovic I. Interactions of gold and silver nanoparticles with bacterial biofilms: molecular interactions behind inhibition and resistance. *Int J Mol Sci*. 2020;21:7658. doi:10.3390/ijms21207658
28. Joshi AS, Bapat MV, Singh P, Mijakovic I. Viridibacillus culture derived silver nanoparticles exert potent anticancer action in 2D and 3D models of lung cancer via mitochondrial depolarization-mediated apoptosis. *Mater Today Bio*. 2024;25:100997. doi:10.1016/j.mtbio.2024.100997
29. Singh P, Pandit S, Garnæs J, et al. Green synthesis of gold and silver nanoparticles from Cannabis sativa (industrial hemp) and their capacity for biofilm inhibition. *Int J Nanomed*. 2018;13:3571–3591. doi:10.2147/IJN.S157958
30. Singh P, Mijakovic I. Harnessing barley grains for green synthesis of gold and silver nanoparticles with antibacterial potential. *Discover Nano*. 2024;19:101. doi:10.1186/s11671-024-04042-4
31. Ielo I, Rando G, Giacobello F, et al. Synthesis, chemical-physical characterization, and biomedical applications of functional gold nanoparticles: a review. *Molecules*. 2021;26:5823. doi:10.3390/molecules26195823
32. Singh P, Pandit S, Mokkapati V, Garnæs J, Mijakovic I. A sustainable approach for the green synthesis of silver nanoparticles from Solibacillus isronensis sp. and their application in biofilm inhibition. *Molecules*. 2020;25:2783. doi:10.3390/molecules25122783
33. Shanmugam J, Dhayalan M, Savaas Umar MR, et al. Green synthesis of silver nanoparticles using Allium cepa var. Aggregatum natural extract: antibacterial and cytotoxic properties. *Nanomaterials*. 2022;12.
34. Singh P, Pandit S, Jers C, et al. Silver nanoparticles produced from Cedecea sp. exhibit antibiofilm activity and remarkable stability. *Sci Rep*. 2021;11:12619. doi:10.1038/s41598-021-92006-4
35. Singh P, Mijakovic I. Antibacterial effect of silver nanoparticles is stronger if the production host and the targeted pathogen are closely related. *Biomedicines*. 2022;10:628. doi:10.3390/biomedicines10030628
36. Zhang J, Singh P, Cao Z, et al. Polydopamine/graphene oxide coatings loaded with tetracycline and green Ag nanoparticles for effective prevention of biofilms. *Appl Surf Sci*. 2023;626:157221. doi:10.1016/j.apsusc.2023.157221
37. Saif S, Tahir A, Chen Y. Green synthesis of iron nanoparticles and their environmental applications and implications. *Nanomaterials*. 2016;6:209. doi:10.3390/nano6110209
38. Jiang Y, Zhou P, Zhang P, et al. Green synthesis of metal-based nanoparticles for sustainable agriculture. *Environ Pollut*. 2022;309:119755. doi:10.1016/j.envpol.2022.119755
39. Samuel MS, Ravikumar M, John JA, et al. A review on green synthesis of nanoparticles and their diverse biomedical and environmental applications. *Catalysts*. 2022;12:459. doi:10.3390/catal12050459
40. Masadeh MM, Bany-Ali NM, Khanfar MS, et al. Synergistic antibacterial effect of ZnO nanoparticles and antibiotics against multidrug-resistant biofilm bacteria. *Curr Drug Deliv*. 2025;22:92–106. doi:10.2174/0115672018279213240110045557
41. Liu H, Zhen Z, Chen F, Chen J, Chen W. Advancements in iron oxide nanoparticles for multimodal imaging and tumor theranostics. *Curr Med Chem*. 2025;32:301–321. doi:10.2174/0109298673301359240705063544
42. Bhagat DS, Gurnule WB, Bumbrah GS, Koinkar P, Chawla PA. Recent advances in biomedical applications of biogenic nanomaterials. *Curr Pharm Biotechnol*. 2023;24:86–100. doi:10.2174/1389201023666220513101628
43. Ko MJ, Min S, Hong H, et al. Magnetic nanoparticles for ferroptosis cancer therapy with diagnostic imaging. *Bioact Mater*. 2024;32:66–97. doi:10.1016/j.bioactmat.2023.09.015
44. Ronavari A, Igaz N, Adamecz DI, et al. Green silver and gold nanoparticles: biological synthesis approaches and potentials for biomedical applications. *Molecules*. 2021;26:844. doi:10.3390/molecules26040844
45. Singh R, Thakur P, Thakur A, et al. Colorimetric sensing approaches of surface-modified gold and silver nanoparticles for detection of residual pesticides: a review. *Int J Environ Anal Chem*. 2021;101:3006–3022. doi:10.1080/03067319.2020.1715382
46. Singh P, Mijakovic I. Rowan berries: a potential source for green synthesis of extremely monodisperse gold and silver nanoparticles and their antimicrobial property. *Pharmaceutics*. 2022;14:82. doi:10.3390/pharmaceutics14010082
47. Julkowska D, Obuchowski M, Holland IB, Seror SJ. Comparative analysis of the development of swarming communities of Bacillus subtilis 168 and a natural wild type: critical effects of surfactin and the composition of the medium. *J Bacteriol*. 2005;187:65–76. doi:10.1128/JB.187.1.65-76.2005
48. Kesel S, Grumbein S, Gümperlein I, et al. Direct comparison of physical properties of Bacillus subtilis NCIB 3610 and B-1 biofilms. *Appl Environ Microbiol*. 2016;82:2424–2432. doi:10.1128/AEM.03957-15
49. Eymard-Vernain E, Luche S, Rabilloud T, Lelong C. Impact of nanoparticles on the Bacillus subtilis (3610) competence. *Sci Rep*. 2018;8:2978. doi:10.1038/s41598-018-21402-0
50. Falcón García C, Kretschmer M, Lozano-Andrade CN, et al. Metal ions weaken the hydrophobicity and antibiotic resistance of Bacillus subtilis NCIB 3610 biofilms. *npj Biofilms Microbiomes*. 2020;6(1). doi:10.1038/s41522-019-0111-8
51. Plaza GA, Chojniak J, Mendrek B, et al. Synthesis of silver nanoparticles by Bacillus subtilis T-1 growing on agro-industrial wastes and producing biosurfactant. *IET Nanobiotechnol*. 2016;10:62–68. doi:10.1049/iet-nbt.2015.0016
52. Kabeerdass N, Al Otaibi A, Rajendran M, et al. Bacillus-mediated silver nanoparticle synthesis and its antagonistic activity against bacterial and fungal pathogens. *Antibiotics*. 2021;10:1334. doi:10.3390/antibiotics10111334
53. Habeeb Rahuman HB, Dhandapani R, Narayanan S, et al. Medicinal plants mediated the green synthesis of silver nanoparticles and their biomedical applications. *IET Nanobiotechnol*. 2022;16:115–144. doi:10.1049/nbt2.12078
54. Singh P, Mijakovic I. Strong antimicrobial activity of silver nanoparticles obtained by the green synthesis in Viridibacillus sp. Extracts. *Front Microbiol*. 2022;13. doi:10.3389/fmicb.2022.820048
55. Mendes CR, Dilarri G, Forsan CF, et al. Antibacterial action and target mechanisms of zinc oxide nanoparticles against bacterial pathogens. *Sci Rep*. 2022;12:2658. doi:10.1038/s41598-022-06657-y
56. Maity S, Sarkar D, Poddar K, Patil P, Sarkar A. Biofilm-mediated heavy metal removal from aqueous system by multi-metal-resistant bacterial strain Bacillus sp. GH-s29. *Appl Biochem Biotechnol*. 2023;195:4832–4850. doi:10.1007/s12010-022-04288-7
57. Khan F, Jeong G-J, Singh P, et al. Retrospective analysis of the key molecules involved in the green synthesis of nanoparticles. *Nanoscale*. 2022;14:14824–14857. doi:10.1039/D2NR03632K

58. Chugh G, Singh BR, Adholeya A, Barrow CJ. Role of proteins in the biosynthesis and functioning of metallic nanoparticles. *Crit Rev Biotechnol*. 2022;42:1045–1060. doi:10.1080/07388551.2021.1985957
59. Park Y, Hong YN, Weyers A, Kim YS, Linhardt RJ. Polysaccharides and phytochemicals: a natural reservoir for the green synthesis of gold and silver nanoparticles. *IET Nanobiotechnol*. 2011;5:69–78. doi:10.1049/iet-nbt.2010.0033
60. Ali IAM, Ahmed AB, Al-Ahmed HI. Green synthesis and characterization of silver nanoparticles for reducing the damage to sperm parameters in diabetic compared to metformin. *Sci Rep*. 2023;13:2256. doi:10.1038/s41598-023-29412-3
61. Duran N, Silveira CP, Duran M, Martinez DS. Silver nanoparticle protein Corona and toxicity: a mini-review. *J Nanobiotechnology*. 2015;13:55. doi:10.1186/s12951-015-0114-4
62. Nye TM, Schroeder JW, Kearns DB, Simmons LA. Complete genome sequence of undomesticated Bacillus subtilis strain NCIB 3610. *Genome Announc*. 2017;5. doi:10.1128/genomeA.00364-17
63. Bremer E, Calteau A, Danchin A, et al. A model industrial workhorse: bacillus subtilis strain 168 and its genome after a quarter of a century. *Microb Biotechnol*. 2023;16:1203–1231. doi:10.1111/1751-7915.14257
64. Moch C, Schrogel O, Allmansberger R. Transcription of the nfrA-ywcH operon from Bacillus subtilis is specifically induced in response to heat. *J Bacteriol*. 2000;182:4384–4393. doi:10.1128/JB.182.16.4384-4393.2000
65. Pramastya H, Song Y, Elfahmi EY, Sukrasno S, Quax WJ. Positioning Bacillus subtilis as terpenoid cell factory. *J Appl Microbiol*. 2021;130:1839–1856. doi:10.1111/jam.14904
66. Platania V, Kaldeli-Kerou A, Karamanidou T, et al. Antibacterial effect of colloidal suspensions varying in silver nanoparticles and ions concentrations. *Nanomaterials*. 2022;12:31. doi:10.3390/nano12010031
67. Shaaban MT, Mohamed BS, Zayed M, El-Sabbagh SM. Antibacterial, antibiofilm, and anticancer activity of silver-nanoparticles synthesized from the cell-filtrate of Streptomyces enissocaesilis. *BMC Biotech*. 2024;24(8). doi:10.1186/s12896-024-00833-w
68. Elangovan D, Rahman HBH, Dhandapani R, et al. Coating of wallpaper with green synthesized silver nanoparticles from Passiflora foetida fruit and its illustrated antifungal mechanism. *Process Biochem*. 2022;112:177–182. doi:10.1016/j.procbio.2021.11.027
69. Bruna T, Maldonado-Bravo F, Jara P, Caro N. Silver nanoparticles and their antibacterial applications. *Int J Mol Sci*. 2021;22:7202. doi:10.3390/ijms22137202
70. Moradi F, Ghaedi A, Fooladfar Z, Bazrgar A. Recent advance on nanoparticles or nanomaterials with anti-multidrug resistant bacteria and anti-bacterial biofilm properties: a systematic review. *Heliyon*. 2023;9:e22105. doi:10.1016/j.heliyon.2023.e22105
71. Hamidian K, Sarani M, Sheikhi E, Khatami M. Cytotoxicity evaluation of green synthesized ZnO and Ag-doped ZnO nanoparticles on brain glioblastoma cells. *J Mol Struct*. 2022;1251:131962. doi:10.1016/j.molstruc.2021.131962
72. Liao S, Zhang Y, Pan X, et al. Antibacterial activity and mechanism of silver nanoparticles against multidrug-resistant Pseudomonas aeruginosa. *Int J Nanomed*. 2019;14:1469–1487. doi:10.2147/IJN.S191340
73. Yuan YG, Peng QL, Gurunathan S. Effects of silver nanoparticles on multiple drug-resistant strains of staphylococcus aureus and pseudomonas aeruginosa from mastitis-infected goats: an alternative approach for antimicrobial therapy. *Int J Mol Sci*. 2017;18:569. doi:10.3390/ijms18030569